

Numerical simulations of forced shallow-water turbulence: effects of moist convection on the large-scale circulation of Jupiter and Saturn

ADAM P. SHOWMAN
University of Arizona, Tucson, AZ

Submitted to *J. Atmos. Sci.*

Corresponding author address:

A.P. Showman, Department of Planetary Sciences, Lunar and Planetary Laboratory, University of Arizona, Tucson, AZ 85721 (showman@lpl.arizona.edu)

ABSTRACT

To test the hypothesis that the zonal jets on Jupiter and Saturn result from energy injected by thunderstorms into the cloud layer, I present forced-dissipative numerical simulations of the shallow-water equations in spherical geometry. The forcing consists of sporadic, isolated circular mass pulses intended to represent thunderstorms; the damping, representing radiation, removes mass evenly from the layer. My results show that the deformation radius provides strong control over the behavior. At deformation radii < 2000 km (0.03 Jupiter radii), the simulations produce broad jets near the equator, but regions poleward of 15-30 degrees latitude instead become dominated by vortices. Simulations at deformation radii > 4000 km (0.06 Jupiter radii), however, become dominated by barotropically stable zonal jets with only weak vortices. The lack of midlatitude jets at small deformation radii results from the suppression of the beta effect by column stretching; this effect has been previously documented in the quasigeostrophic system but never before in the full shallow-water system. In agreement with decaying shallow-water turbulence simulations, but in disagreement with Jupiter and Saturn, the equatorial flows in my forced simulations are always westward. In analogy with purely two-dimensional turbulence, the size of the coherent structures (jets and vortices) depends on the relative strengths of forcing and damping; stronger damping removes energy faster as it cascades upscale, leading to smaller vortices and more closely spaced jets in the equilibrated state. Forcing and damping parameters relevant to Jupiter produce flows with speeds up to 50-200 m/sec and a predominance of anticyclones over cyclones, both in agreement with observations. However, the dominance of vortices over jets at deformation radii thought to be relevant to Jupiter (1000-3000 km) suggests either that the actual deformation radius is larger than previously believed or that three-dimensional effects, not included in the shallow-water equations, alter the dynamics in a fundamental manner.

1. Introduction

The large-scale circulation and banded appearance of Jupiter and Saturn have been major puzzles since high-resolution images of these planets were returned by the Voyager and Pioneer spacecraft in the 1970s. Salient features include numerous zonal jets (~ 30 on Jupiter and ~ 20 on Saturn); strong prograde (eastward) equatorial flows, peaking at $\sim 150 \text{ m sec}^{-1}$ on Jupiter and $\sim 400 \text{ m sec}^{-1}$ on Saturn; and numerous coherent vortices ranging in size from the limit of image resolution (tens of km) to Jupiter's Great Red Spot (dimensions $20,000 \times 10,000 \text{ km}$). About 90% of compact vortices on Jupiter are anticyclones (Li et al. 2004; Mac Low and Ingersoll 1986). Despite the presence of the vortices, the jets are remarkably stable in time, show minimal meandering in longitude, and contain most of the kinetic energy. Importantly, although the banded appearance of the planet extends only to latitudes $\sim 50^\circ$, the zonal jets extend to at least 85° latitude (Porco et al. 2003). The jets violate the barotropic stability criterion by up to a factor of ~ 3 (Ingersoll et al. 1981), although they may be close to neutral stability with respect to Arnol'd's second stability criterion (Dowling 1995). A successful model must account for all these features.

Many authors have suggested that the zonal jets are produced when small-scale turbulence injected into the cloud layer undergoes an inverse energy cascade modified by the β effect (Cho and Polvani 1996a, b; Williams 1978). Thunderstorms, which have been observed by Voyager, Galileo, and Cassini, provide a leading candidate for such turbulence (Gierasch et al. 2000; Ingersoll et al. 2000). However, with the exception of a recent quasigeostrophic study by Li et al. (2006), numerical models with realistic thunderstorm turbulence have not been performed. On Jupiter and Saturn, thunderstorms are localized, episodic, and cover only a small fraction ($< 1\%$) of the planet's area (Little et al. 1999; Porco et al. 2003). In contrast, most two-dimensional turbulence studies use random forcing that occurs everywhere simultaneously and is confined to a small range of wavenumbers. This shortcoming prevents a robust assessment of jet formation in the giant-planet context.

Furthermore, most published turbulence investigations that focus on jets have been

purely two-dimensional, hence precluding the vortex stretching (and associated horizontal divergence) that can be crucial in atmospheres (Vasavada and Showman 2005). These two-dimensional studies have generally shown that zonal jets with a characteristic width of $\sim (U/\beta)^{1/2}$, where U is the characteristic wind speed and β is the gradient of planetary vorticity, can result from forced turbulence (Galperin et al. 2006; Huang and Robinson 1998; Huang et al. 2001; Nozawa and Yoden 1997; Sukoriansky et al. 2007; Williams 1978). However, recent quasigeostrophic studies have demonstrated that, in the presence of vortex stretching (i.e., finite deformation radius), the Rhines scale can differ radically from $(U/\beta)^{1/2}$ (Okuno and Masuda 2003; Smith 2004; Theiss 2004) or even be suppressed entirely. Despite the relevance of these studies, the asymptotic expansions that underlie the quasigeostrophic equation still confine the dynamics to a particular regime of parameter space; such studies exclude full column stretching, buoyancy (gravity) waves, cyclone-anticyclone asymmetry, and many other phenomena that may be relevant to Jupiter and Saturn.

The simplest atmospheric model that allows large-amplitude column stretching is the shallow-water model. In contrast to the quasigeostrophic system (which restricts vertical stretching to small fractional amplitude), fluid columns in shallow water can undergo order-unity changes in vertical thickness; however, baroclinic effects such as column twisting and tilting are excluded. There exist several decaying (Arai and Yamagata 1994; Farge and Sadourny 1989; Polvani et al. 1994; Spall and McWilliams 1992) and forced (Yuan and Hamilton 1994) shallow-water turbulence investigations on the f -plane that investigate the interaction between slow-moving vortex structures and high-frequency gravity waves. However, only a few turbulent shallow-water investigations have been published that focus on jets, and all of these investigated decaying rather than forced turbulence (Cho and Polvani 1996a, b; Iacono et al. 1999a, b; Peltier and Stuhne 2002). No *forced* shallow-water turbulence simulations have yet been published that include the β effect necessary for jet formation.

Here, I present numerical simulations addressing the question of whether Jupiter-like jets and vortices can spontaneously result from forced-dissipative shallow-water turbulence

with a realistic representation of thunderstorm pumping. The primary goal is to determine the relevance of the forced shallow-water model to Jupiter and Saturn; a secondary motivation is to shed light on the inherent dynamics of the forced shallow-water system in the presence of β . Section 2 describes the model, and Sections 3–5 describe the basic flow regime, energetics, and diagnostics. Section 6 compares the results to the giant planets, and Section 7 concludes.

2. Model

Available constraints suggest that Jupiter’s atmosphere contains a statically stable upper troposphere overlying a neutrally stable convecting interior. We adopt a two-layer model, with constant densities in each layer, where the lower layer represents the neutrally stratified deep interior and the upper layer represents the statically stable, buoyant “weather layer” in the upper troposphere. In the limit where the lower layer becomes infinitely deep and the lower-layer winds and pressure gradients remain steady with time (which requires the upper layer to be isostatically balanced), this two-layer system reduces to the shallow-water equations for the flow in the upper layer (Dowling and Ingersoll 1989; Gill 1982):

$$\frac{du}{dt} - \frac{uv \tan \phi}{a} = -\frac{g}{a \cos \phi} \frac{\partial h}{\partial \lambda} + fv \quad (1)$$

$$\frac{dv}{dt} + \frac{u^2 \tan \phi}{a} = -\frac{g}{a} \frac{\partial h}{\partial \phi} - fu \quad (2)$$

$$\frac{d(gh)}{dt} = -gh \nabla \cdot \mathbf{v} + S_{\text{storm}} + S_{\text{rad}} \quad (3)$$

where $u(\lambda, \phi, t)$ and $v(\lambda, \phi, t)$ are the eastward and northward speeds; $h(\lambda, \phi, t)$ is the thickness of the upper layer; λ , ϕ , and t are longitude, latitude, and time; $f = 2\Omega \sin \phi$ is the Coriolis parameter; a is the planetary radius; and g is the reduced gravity (equal to the actual gravity times the fractional density difference between layers). We take the height variable to be gh , since g and h only ever appear in this combination. The shallow-water layer represents

the mass above a surface of constant potential density (virtual potential temperature) near the water-condensation level at $\sim 5\text{--}10$ bars. $S_{\text{storm}}(\lambda, \phi, t)$ and $S_{\text{rad}}(\lambda, \phi, t)$ represent mass sources and sinks associated with thunderstorms and radiation.

In the general case where the deep (abyssal) layer contains prescribed winds, an additional term (mathematically equivalent to a topography term) must be added to Eqs. 1–2 (Dowling and Ingersoll 1989). In this study, however, I assume that the abyssal layer is motionless, so no such term need be added. The model therefore represents a shallow baroclinic flow with no barotropic mode.

The shallow-water equations differ from the barotropic equations in having a finite deformation radius, $L_d = \sqrt{gh}/f$. In the context of the two-layer model, this corresponds to an internal deformation radius associated with static stability in the upper troposphere. Modeling studies of Jupiter’s Great Red Spot (latitude 27°S) indicate that $L_d \sim 1000\text{--}2000$ km (Cho et al. 2001; Marcus 1988); values even a factor of two higher precluded these models from reproducing realistic behavior of the vortex. These constraints on deformation radius are consistent with direct measurements of static stability by the Galileo Probe (Magalhães et al. 2002) from 1–22 bars and estimates from condensation of water in the 1–10 bar layer (Achterberg and Ingersoll 1989; Nakajima et al. 2000). Here we treat L_d as a free parameter but focus on midlatitude values 1000–2000 km relevant to Jupiter. Given Jupiter’s rotation rate $\Omega = 1.74 \times 10^{-4} \text{ sec}^{-1}$, this implies layer thicknesses $gh \sim 0.5\text{--}1 \times 10^5 \text{ m}^2 \text{ sec}^{-2}$.

Thunderstorms transport mass from the deep interior to the neutral-buoyancy level in the upper troposphere. On Jupiter, lightning occurs within opaque, bright cloud features that expand to diameters up to $\sim 1000\text{--}5000$ km in a few days (Banfield et al. 1998; Gierasch et al. 2000; Porco et al. 2003). The small-scale convective processes that determine the lifetimes and sizes of these storms remain poorly understood; here, I simply parameterize the storm mass transport by adding localized, episodic mass pulses to the weather layer:

$$S_{\text{storm}} = \sum s_{\text{storm}} \quad (4)$$

Each mass pulse is represented as a circular gaussian in space and time:

$$s_{\text{storm}} = s_{\text{max}} \exp \left[-\frac{r^2}{r_{\text{storm}}^2} - \frac{(t - t_0)^2}{\tau_{\text{storm}}^2} \right] \quad (5)$$

where r_{storm} is the storm radius, r is the distance on the sphere between the specified storm center (different for each storm) and a given longitude and latitude, t_0 is the time at which the storm peaks, τ_{storm} is the characteristic storm lifetime, and s_{max} is peak mass injection rate at the storm center. Physically, the idea is that latent heat release and rainout increases the potential temperature of the thunderstorm air, allowing it to enter the weather layer and form an anvil at the neutral-buoyancy level.

Storms, represented by Eq. 5, are injected randomly in time throughout the simulation, with an average time interval between storms of τ_{interval} . For most of the simulations, the storm locations were randomly chosen so that the average number of storms that occur per unit area per unit time is independent of latitude (which implies that the number density of storms per unit latitude scales as $\cos \phi$). For any given storm, the gaussians in Eq. 5 were truncated to zero at distances $\geq 2.2r_{\text{storm}}$ and times $|t - t_0| \geq 2.2\tau_{\text{storm}}$. During any given storm, the location of mass injection was kept constant in time (i.e., the locations of mass injection do not advect with the weather-layer flow), which is consistent with the assumption that the storms are rooted in the (motionless) abyssal layer.

To summarize, the thunderstorm parameterization entails four free parameters — the storm size r_{storm} , lifetime τ_{storm} , amplitude s_{max} , and spacing in time τ_{interval} . These parameters were the same for all storms in a given simulation. I explore a wide range of values, but emphasize values relevant for Jupiter and Saturn. Nominal values, motivated by observations, are $r_{\text{storm}} = 870\text{--}2600$ km ($0.7\text{--}2^\circ$), $\tau_{\text{interval}} = 10^5$ sec, and $\tau_{\text{storm}} = 10^5$ sec. This choice of τ_{storm} ensures that most of the injected energy enters the balanced flow rather than driving gravity waves. The amplitude s_{max} is the least-well constrained parameter observationally; I explore values between 0.0033 and $10 \text{ m}^2 \text{ sec}^{-3}$.

Thunderstorms add mass to the weather layer, which on a giant planet would cause

isentropes to migrate downward. In contrast, radiation cools the atmosphere, causing isentropes to migrate upward. This is equivalent to a mass sink. Thus, radiation is modeled by removing mass from the layer. I use a simple relaxation scheme:

$$\frac{S_{\text{rad}}}{g} = -\frac{\langle h \rangle - h_{\text{eq}}}{\tau_{\text{mass}}} - \frac{h - \langle h \rangle}{\tau_{\text{APE}}} \quad (6)$$

where h_{eq} is a specified, constant equilibrium thickness and $\langle h \rangle$ is the instantaneous spatially averaged h . The first term relaxes the mean thickness toward h_{eq} over a timescale τ_{mass} ; this term removes mass without affecting the energy. In contrast, the second term flattens thickness variations over a timescale τ_{APE} , which removes available potential energy (APE) without affecting the layer mass. (Physically, this is equivalent to letting hot regions undergo faster cooling than cold regions.) Together, the terms allow a statistical steady state in mass and energy to be established with the forcing. (Note that when τ_{mass} equals τ_{APE} , Eq. 6 collapses to the standard Newtonian-relaxation scheme $S_{\text{rad}}/g = -(h - h_{\text{eq}})/\tau$.) Generally, h_{eq} was chosen so that the flow equilibrated to a layer thickness that yielded the desired value of L_d . τ_{mass} is not a free parameter; usually it was chosen to be a short value (say 10^6 sec) so that the layer was forced to maintain an average thickness close to h_{eq} . I explored values of τ_{APE} from 10^7 sec to infinity.

Note that the momentum equation contains no sources or sinks. Because giant planets have no solid surfaces to cause friction, we do not include a drag term in Eqs. 1–2; instead, the APE removal term in Eq. 6 provides the sole source of damping (aside from hyperviscosity necessary for numerical stability). Our exclusion of small-scale forcing in the momentum equation is equivalent to the assumption that any small-scale convective kinetic energy (e.g., in thunderstorm updrafts) does not couple to the large-scale flow represented by the shallow-water equations but instead dissipates locally at small scales. Rather, we envision that the pressure gradients associated with the mass pulses provide the sole source of flow acceleration at large scales. While this is probably an oversimplification, it provides a first step in understanding the influence of convection on the flow. A key point here is that the

forcing is *unbalanced* and represents only the thermal perturbations caused by the convection; the gravitational (e.g., geostrophic) adjustment of these perturbations is explicitly simulated. These mass perturbations are effectively the thunderstorm anvils, which on Jupiter are large enough to be governed by hydrostatic, quasi-two-dimensional flow (Hueso et al. 2002).

I solved Equations 1–3 in spherical geometry using the Explicit Planetary Isentropic Coordinate (EPIC) model (Dowling et al. 1998), which discretizes the equations on a longitude-latitude Arakawa C-grid and adopts 3rd-order Adams-Bashforth stepping in time. The mass advection uses the scheme of Hsu and Arakawa (1990). The original version of EPIC attempted to merge this scheme with the Adams-Bashforth timestepper, which led to an ill-conceived scheme for updating the values of h in the continuity equation (Eq. 18 from Dowling et al. (1998)) that spuriously multiplied the mass source by a factor of 23/12. This error has been fixed.

The simulations are performed on a portion of a sphere with Jupiter’s radius ($a = 7.14 \times 10^7$ m) and rotation rate ($\Omega = 1.74 \times 10^{-4}$ sec $^{-1}$). The standard domain is 120° in longitude and 0–70° in latitude, with periodic and channel (i.e., free-slip wall) boundary conditions, respectively. A few simulations were run with domains extending 360° in longitude or pole-to-pole in latitude to confirm that the results do not depend on the choice of domain. The initial condition consists of a flat layer at rest, with an initial thickness generally equal to h_{eq} . The standard resolution is 512×298 or 256×149 , corresponding to 0.23° (290 km) or 0.46° (580 km) per gridpoint at the equator. (The low-resolution runs generally used storm radii of 2°. Smaller storm radii of 0.7° were only used in high-resolution runs. These choices ensured that at least 6–8 grid points spanned a storm diameter in all cases.) The timestep ranged between 2 and 20 sec, depending on the layer thickness. The equations included a ∇^4 hyperviscosity to maintain numerical stability. The simulations were generally run for 3000–10,000 Earth days (7000–20,000 Jupiter rotations).

Table 1 lists the runs presented in the figures, which represent a fraction of the total runs performed. Sequence A corresponds to continually accelerating flows ($\tau_{\text{APE}} \rightarrow \infty$). Sets D1

and D2 explore the effects of damping (τ_{APE}) when other parameters are held fixed. Set F explores the effect of varying the forcing strength, s_{max} , when damping and other parameters are held fixed. Set C corresponds to simulations with *negative* mass pulses ($s_{\text{max}} < 0$), which are useful in quantifying the cyclone-anticyclone asymmetry. Finally, set E presents some additional runs used to round out the energy statistics.

3. Basic flow regime: Suppression of the Rhines effect at small deformation radius

Under Jovian conditions, geostrophic adjustment of the injected mass pulses produces a population of small vortices, primarily anticyclones, with typical speeds of $\sim 10\text{--}100 \text{ m sec}^{-1}$ depending on the forcing parameters. These vortices rapidly grow by merger, indicating a robust inverse cascade that drives energy toward large scales. The existence of an inverse cascade in these simulations is consistent with previous work (Cho and Polvani 1996b; Polvani et al. 1994; Yuan and Hamilton 1994), with the exception that, unlike previous shallow-water, quasigeostrophic, or two-dimensional turbulence investigations, the forcing here is unbalanced. In my simulations, the detailed behavior depends strongly on the deformation radius and to a lesser degree on the forcing and damping parameters; here we describe the range of behavior before proceeding to parameter variations and detailed diagnostics.

One of my key results is that when the midlatitude deformation radius is small ($< 2000 \text{ km}$), the flow develops broad equatorial jets, but the midlatitudes become dominated by vortices rather than jets. These phenomena are illustrated in Fig. 1, which depicts the thickness (greyscale) and winds (arrows) for a simulation with midlatitude $L_d \sim 1200 \text{ km}$, relevant to Jupiter. A broad westward jet forms at the equator and a flanking eastward jet forms at a latitude of $\sim 15\text{--}30^\circ$, depending on the parameters. In Fig. 1, the energy damping is turned off ($\tau_{\text{APE}} \rightarrow \infty$), so the jets grow larger over time as the flow accelerates (they widen from $\sim 15^\circ$ latitude at 600 days to $\sim 30^\circ$ latitude at 4000 days in Fig. 1). In simulations with finite τ_{APE} , however, these equatorial jets equilibrate at a finite width. The potential vorticity

(pv) becomes almost homogenized in the latitudinal strip containing the equatorial jets, which is evident in Fig. 2. This explains the emergence of only two equatorial jets, westward at the equator and eastward at 15–30° latitude; multiple jets would require non-homogenized pv , which does not occur at low latitudes in these simulations. Such homogenization of pv at the equator may be relevant to the giant planets (Allison et al. 1995).

TABLE 1.

The fact that the midlatitudes becomes dominated by vortices rather than jets (Figs. 1–2) contrasts with two-dimensional forced simulations, which produce jets with relative ease (Huang and Robinson 1998; Marcus et al. 2000; Nozawa and Yoden 1997). However, my result agrees with recent quasigeostrophic investigations (Okuno and Masuda 2003; Smith 2004; Theiss 2004) showing that finite deformation radius can inhibit the β effect. The Rossby-wave dispersion relation can be written as

FIG. 1.

FIG. 2.

$$\omega = -\frac{\beta k_x}{k_x^2 + k_y^2 + k_d^2} \quad (7)$$

where k_x and k_y are the zonal and meridional wavenumbers of the Rossby wave, k_d is the wavenumber associated with the deformation radius, and β is the gradient of the Coriolis parameter. The Rhines scale is obtained by equating this frequency with the turbulence frequency $U|k|$, which yields a modified Rhines scale

$$k_R^2 = \frac{\beta}{U} |\cos \theta| - k_d^2 \quad (8)$$

where k_R is the Rhines wavenumber, U is a characteristic wind speed and θ is the angle between the Rossby-wave propagation direction and east. The finite deformation radius decreases the Rossby-wave frequency, which moves the Rhines wavenumber to smaller values. Clearly, if k_d is large enough, the Rhines wavenumber shrinks to zero, which implies that all wavenumbers are turbulence dominated. In this case, the Rhines wavenumber does not exist and the flow is governed by isotropic turbulence in the presence of finite deformation radius. Previous studies documenting this phenomenon have been quasigeostrophic (Okuno and Masuda 2003; Smith 2004; Theiss 2004); the present study — along with an independent

investigation performed simultaneously by Scott and Polvani (2006) — is the first time that suppression of β by finite deformation radius has been clearly observed in the full shallow-water equations.

These ideas can be further illustrated with the vorticity equation, which for shallow water can be written (neglecting forcing)

$$\frac{\partial \zeta}{\partial t} + \mathbf{v} \cdot \nabla \zeta + v\beta + (\zeta + f)\nabla \cdot \mathbf{v} = 0 \quad (9)$$

where ζ is relative vorticity and v is meridional wind speed. In purely two-dimensional turbulence, the divergence term is zero, and the $v\beta$ term competes for dominance with the nonlinear advection term [the crossover occurring at the Rhines wavenumber relevant for two-dimensional turbulence, $(\beta/U)^{1/2}$]. However, the horizontal compressibility (nonzero $\nabla \cdot \mathbf{v}$) introduced in the shallow water equations implies that, under some circumstances, the divergence term can overwhelm the $v\beta$ term, thereby weakening or nullifying the influence of β . In particular, the divergence term is large when the deformation radius is small. Therefore, when the deformation radius becomes small enough, the β effect can be suppressed, preventing the formation of jets and leading to quasi-isotropic turbulence instead (Okuno and Masuda 2003).

My simulations exhibit hybrid behavior, with jets near the equator and vortices in midlatitudes. The above framework naturally explains this dual behavior. On a spherical planet, the deformation radius ranges from large near the equator to a minimum at the poles. Therefore, a critical latitude can exist below which jets form and above which they cannot (Theiss 2004). The expression for the predicted critical latitude is obtained by setting k_R to zero in Eq. 8. Using $f = 2\Omega \sin \phi$, $\beta = 2\Omega \cos \phi/a$ as appropriate to spherical geometry, and $L_d = \sqrt{gh}/f$ as appropriate away from the equator, we obtain

$$\cos \phi_{\text{crit}} = -\frac{gh}{4U\Omega a} + \left[\frac{1}{16} \left(\frac{gh}{U\Omega a} \right)^2 + 1 \right]^{1/2} \quad (10)$$

where U is the wind speed and a is the planetary radius. Defining a global Rossby number $Ro_a = U/(\Omega a)$ and the Froude number $F = U/\sqrt{gh}$, we can write Eq. 10 as

$$\cos \phi_{\text{crit}} = -\frac{Ro_a}{4F^2} + \left[\frac{1}{16} \frac{Ro_a^2}{F^4} + 1 \right]^{1/2} \quad (11)$$

Although Eqs. 10–11 result from scaling arguments and are probably not quantitatively precise, it is nevertheless interesting to compare this prediction with our simulations. As pointed out by Theiss (2004), the interaction of Rossby waves and turbulence that leads to Eq. 8 is local, so the best way to make this comparison is to use the *local* Ro_a and F in a given simulation to determine the predicted critical latitude for that simulation. We do this by zonally averaging the zonal wind, u , and layer thickness, gh , and using them to compute latitudinally varying Ro_a , F , and hence trial ϕ_{crit} through Eq. 11. If Eq. 11 is valid, we would expect jets to dominate at latitudes where this trial $\phi_{\text{crit}}(\phi)$ exceeds the actual latitude ϕ and vortices to dominate at latitudes where $\phi_{\text{crit}}(\phi)$ is less than ϕ . The crossover point corresponds to the predicted critical latitude for that simulation, with a corresponding value of $Ro_a F^{-2} = gh/u\Omega a$ at that latitude. Fig. 3 plots the actual critical latitude, as obtained from the simulations, against the predicted critical latitude computed in this manner. The actual critical latitudes were determined by visual inspection from plots of the layer thickness and winds.

The results (Fig. 3) show good agreement between the prediction and the simulations when the actual critical latitude is ~ 10 – 25° , but the prediction substantially underestimates the critical latitude for simulations where the observed transition between jets and vortices occurs at ~ 25 – 40° latitude (e.g., the last panel of Fig. 1). None of my simulations produce critical latitudes less than ~ 6 – 8° latitude; instead, the equatorial jet forms directly at finite width (e.g., see first three panels of Fig. 1). This may be related to the finite size of the mass pulses introduced in the forcing.

At first glance, the suppression of jet formation at small deformation radius appears to contradict the results of Cho and Polvani (1996b), who reported the formation of robust zonal

FIG. 3.

FIG. 4.

FIG. 5.

jets when $Ro \ll 1$ and the deformation radius is small compared to the planetary radius. However, careful inspection of their Figs. 11 and 17, where the polar deformation radius was 2000 km ($L_d/a \approx 0.03$) indicates that jets dominate the flow only equatorward of $\sim 45^\circ$ latitude, with vortex domination occurring poleward of $\sim 45^\circ$. These results are consistent with those presented here.

The midlatitude flow becomes more zonal as the deformation radius is increased, although none of my simulations produce regular, Jupiter-like jets in the weather layer. Figures 4–5 illustrate this effect for a simulation with a domain-averaged gh value of $9 \times 10^5 \text{ m}^2 \text{ sec}^{-2}$, implying midlatitude deformation radii of nearly 5000 km. As in the thin-layer cases shown in Figs. 1–2, the injected mass pulses produce small anticyclones (Fig. 4), although these tend to lose energy to gradual wave radiation (for example, notice that the top leftmost vortex in the first panel develops an extensive high-pressure tail extending westward from the main vortex in the second panel). Nevertheless, the coherent structures increase in size over time (third panel), and the final state contains alternating zonal jets with superposed eddy activity (bottom panel).

When jets form in my simulations (e.g., Figs. 4–5), they are always barotropically stable. This is indicated in the top panel of Fig. 5, which shows potential vorticity contours for a flow containing several jets with speeds of $\sim 10 \text{ m sec}^{-1}$. The contours show that pv monotonically increases with latitude, implying that the jets satisfy the Charney-Stern stability criterion. In this simulation, the latitudinal variation of pv is dominated by the latitudinal variation of absolute vorticity. This implies that $\partial^2 \bar{u} / \partial y^2 < \beta$ everywhere, where y is northward distance and the overbar indicates a zonal average. In contrast, many of my vortex-dominated flows (e.g., Figs. 1–2) develop profiles of $\bar{pv}(\phi)$ that vary non-monotonically with latitude at the latitudes of the vortices. Such non-monotonic distributions violate the Charney-Stern criterion, but the criterion is irrelevant to this situation since this pv distribution results from zonal averages through vortices rather than from zonally symmetric jets.

All of my simulations develop westward flow at the equator. This is consistent with

decaying shallow-water investigations on the sphere (Cho and Polvani 1996a, b; Iacono et al. 1999a; Peltier and Stuhne 2002). Consistent with Iacono et al. (1999a), I find that the strength of the westward flow (relative to the midlatitude flow) becomes greater as the fractional height variations become large. The fact that the equatorial jets on Jupiter and Saturn flow eastward suggests that baroclinic processes, not included in the shallow-water system, are important in producing these features.

Next, we consider some diagnostics for further quantifying the extent to which the flow becomes zonal. First we consider spatial heterogeneity: how much variation in flow properties occurs along the zonal direction? One way to quantify this spatial “zonalization” is to compare variations in longitude to variations averaged across the entire domain. We do this by defining the ratio

$$\frac{X_{\text{rms,zonal}}(\phi)}{X_{\text{rms, domain}}} = \frac{\left(\frac{1}{\Delta\lambda} \int (X - \overline{X})^2 d\lambda\right)^{1/2}}{\left(\frac{1}{A} \int (X - \langle X \rangle)^2 dA\right)^{1/2}} \quad (12)$$

where X is any quantity, \overline{X} and $\langle X \rangle$ are the zonal and domain averages of X , respectively, $\Delta\lambda$ is the longitudinal width of the domain, and A is the total area of the domain. The top integral is performed over longitude and the bottom integral is performed over area. The numerator gives the root-mean-square value of the deviations of X in longitude from its zonal average. The denominator gives the root-mean-square value of the deviations of X from its *domain* average.

FIG. 6.

Figure 6 displays this ratio for the zonal wind u , layer thickness h , potential vorticity $(\zeta + f)/gh$, and relative vorticity ζ for simulations with midlatitude deformation radii of 1200 km (solid), 3000 km (dash-dot), and 5000 km (dotted). At all latitudes for the larger two deformation radii, and at latitudes $\sim 0\text{--}40^\circ$ for the smallest deformation radius, the flow becomes quite zonal, with zonal to domain-averaged rms ratios of u and h of $\sim 0.1\text{--}0.5$ and of potential vorticity of $\sim 0.03\text{--}0.2$. (Potential vorticity differs from u and h , especially at the larger two deformation radii, in that its domain-averaged rms value is dominated by the latitude dependence of planetary vorticity rather than by flow-induced variations in latitude.)

FIG. 7.

Only at latitudes poleward of $\sim 40^\circ$ at the smallest deformation radius is the flow not zonal, with zonal to domain-averaged rms ratios of 0.6–2.5 for u , h , and pv . These order-unity values result from the dominance of vortices at high latitudes for the smallest deformation radius.

Interestingly, the relative vorticity becomes less zonalized than the other flow variables (Fig. 6d). This results from the fact that relative vorticity involves derivatives of u and v , so small-scale features have greater signature in ζ than in u , v , or h . The forcing ensures a constant population of small-scale vortices whose signature in ζ has a magnitude similar to those of larger structures despite the fact that the larger structures dominate over the small vortices in u , v , and h (see, e.g., Fig. 2).

Next we consider the flow anisotropy. A standard measure of anisotropy (Rhines 1975; Yoden and Yamada 1993) is $v_{\text{rms}}/u_{\text{rms}}$, where

$$u_{\text{rms}} = \left(\frac{1}{\Delta\lambda} \int u^2 d\lambda \right)^{1/2} \quad (13)$$

and a similar equation holds for v_{rms} . Figure 7 depicts this ratio for simulations at small, medium, and large midlatitude L_d . The figure shows that the flow is relatively isotropic at early times, but that over time the zonal velocities grow to exceed the meridional velocities by a factor of ~ 2 at most latitudes. Nevertheless, for all three simulations there exist latitudes at which $v_{\text{rms}}/u_{\text{rms}} > 1$; generally these correspond to latitudes where vortices reside or where the zonal-mean velocity passes through zero. The ratio of $v_{\text{rms}}/u_{\text{rms}}$ remains close to (or greater than) unity over a wide range of latitudes ($35\text{--}70^\circ$) for the smallest deformation radius; this is an indication of the predominance of relatively isotropic vortices at these latitudes. In contrast, the same simulation reaches $v_{\text{rms}}/u_{\text{rms}}$ values as low as 0.2 from $0\text{--}20^\circ$ latitude, indicating the predominance of the equatorial jet there.

Finally, we consider some basic diagnostics of the zonal-mean flow. If we write variables as the sum of zonal-mean and eddy components, $u \equiv \bar{u} + u'$ and $v \equiv \bar{v} + v'$, insert these definitions into the zonal momentum equation, and then zonally average, we obtain the Eulerian-mean momentum equation for the shallow-water system, given in spherical

coordinates as

$$\frac{\partial \bar{u}}{\partial t} = f\bar{v} - \frac{1}{a \cos^2 \phi} \frac{\partial(\overline{u'v'} \cos^2 \phi)}{\partial \phi} + \frac{\bar{u}\bar{v} \tan \phi}{a} - \frac{\bar{v}}{a} \frac{\partial \bar{u}}{\partial \phi} \quad (14)$$

On the right side, the terms represent zonal accelerations associated with the mean-meridional circulation (first term), meridional convergence of eddy momentum (second term), planetary curvature (third term), and meridional advection (fourth term). For the parameters relevant here, the third and fourth terms are ~ 100 times smaller than the first two terms. Therefore, the primary accelerations of the mean flow result from the eddies and the Coriolis acceleration on the mean-meridional circulation (which, of course, also results indirectly from the effects of eddies).

Figure 8 shows the zonal-mean zonal wind (left) and acceleration terms (right) for the same simulation as in Figs. 1–2, at two different times — early in the top row and late in the bottom row. In the right panels, the solid curves give $-(a \cos^2 \phi)^{-1} \partial(\overline{u'v'} \cos^2 \phi)/\partial \phi$ and the dashed-dot curves give $f\bar{v}$, each averaged over 3-year intervals. The figure illustrates several key points. First, there exists an approximate correlation between the sign of the eddy-momentum convergence and the sign of the zonal winds. In the bottom row, for example, the westward flow from 0 – 25° latitude experiences a westward eddy-momentum convergence, the eastward jet at 25 – 37° experiences an eastward eddy-momentum convergence, the westward flow from 40 – 55° experiences a westward eddy-momentum convergence, and the eastward flow poleward of 55° experiences an eastward eddy-momentum convergence. This confirms our expectations that the injected small-scale eddies pump momentum up-gradient, which drives the large-scale flow.

Second, there is an impressive anti-correlation between the eddy-momentum convergence $-(a \cos^2 \phi)^{-1} \partial(\overline{u'v'} \cos^2 \phi)/\partial \phi$ and the Coriolis acceleration on the mean-meridional flow $f\bar{v}$ (solid and dashed-dot curves, respectively, in the right panels of Fig. 8). This result, which holds true for many of my simulations, indicates that the net acceleration is far weaker than either of these terms in isolation. Although each acceleration is ~ 1 – $4 \times 10^{-6} \text{ m sec}^{-2}$, their near cancellation implies that the net acceleration is typically ~ 5 – 10 times smaller.

The sum of the two accelerations is only a few $\times 10^{-7}$ m sec $^{-2}$ at most latitudes, reaching $\sim 10^{-6}$ m sec $^{-2}$ in the equatorial jet at early times. Crudely, these numbers are consistent with the rate at which the equatorial-jet speed increases in my simulation: a constant acceleration of 10^{-6} m sec $^{-2}$ would imply that the jet would reach a speed of ~ 30 m sec $^{-1}$ after 1 year. At late times, the cancellation becomes better near the equator, and the equatorial jet speed then increases more slowly.

The values of eddy-momentum acceleration depicted in Fig. 8 are similar to values inferred on Jupiter and Saturn from cloud-tracking observations (Del Genio et al. 2007; Ingersoll et al. 1981; Salyk et al. 2006). These authors show that the observed $\overline{u'v'}$ has the correct sign for pumping momentum up-gradient into the jets, and that the typical differences in $\overline{u'v'}$ across jets of width ~ 5000 km is $\sim 5\text{--}20$ m 2 sec $^{-2}$. This implies an eddy-momentum acceleration $\overline{u'v'}/\Delta y \sim 1\text{--}5 \times 10^{-6}$ m sec $^{-2}$. My values are also extremely similar to values obtained by Williams (2003) in 3D primitive-equation simulations driven by baroclinic instabilities (which resulted from imposed thermal contrasts). His figures 8, 10, 12, and 14 also show typical differences in $\overline{u'v'}$ of $\sim 10\text{--}20$ m 2 sec $^{-2}$ across jets of width $\Delta y \sim 6000$ km, again implying an eddy-momentum acceleration $\overline{u'v'}/\Delta y \sim 2\text{--}4 \times 10^{-6}$ m sec $^{-2}$. These agreements suggest that the forcing in my simulations has approximately the correct strength.

In my shallow-water simulations, the nonzero \bar{v} implies latitudinal mass transport. In simulations with large-scale APE damping, this transport balances the mass addition/removal by the damping, allowing the height field to reach a steady state. In simulations without damping, however, this transport causes the height variations to increase over time in the fluid. Such increases are evident in Fig. 1.

My finding that jets are suppressed at small deformation radius disagrees with the results of Li et al. (2006), who reported the formation of robust zonal jets over a broad range of deformation radii — as small as 1000 km — in a one-layer quasigeostrophic model under Jovian conditions. The meridional jet scale in their simulations was typically 5000 km, implying that some of their reported simulations with jets had deformation radii much less than

the jet scale. Their result is puzzling given the known suppression of jets at small deformation radius in one-layer quasigeostrophic models (Okuno and Masuda 2003; Smith 2004; Theiss 2004). The cause of the discrepancy is unclear. Li et al. (2006) present full flow fields only for simulations with $L_d = 5000$ km (their Figs. 1–3), which are broadly consistent with the $L_d = 5000$ km cases presented here. It is possible that their cases with $L_d = 1000$ – 2000 km become vortex dominated, consistent with my Figs. 1–2, but simply develop nonzero $\bar{u}(\phi)$ patterns. (Even at $L_d = 5000$ km, their flows have substantial eddy activity, with $\sim 50\%$ variations in streamfunction along latitude circles.) It is worth emphasizing that the zonal-velocity profile \bar{u} can be strongly nonzero even in such a vortex-dominated flow (cf Fig. 2). Nevertheless, it is also possible that their forcing, which corresponds to intermittent injection of isolated vortices in cyclonic regions, affects the dynamics in a nontrivial manner that promotes the formation of jets over vortices.

FIG. 8.

4. Effect of damping and forcing

a. Energy cycle

We now consider the flow energies and their dependence of the forcing and damping parameters. Figure 9 depicts the total kinetic and available potential energies in the flow for three simulations that are identical except for the value of τ_{APE} , which is ∞ , 10^8 sec, and 10^7 sec from the top to bottom panels, respectively. Here, the kinetic and available potential energies are defined as

$$E_K = \frac{1}{2} \int gh(u^2 + v^2) dA \quad (15)$$

$$E_{\text{APE}} = \frac{1}{2} \int (g\eta)^2 - \langle g\eta \rangle^2 dA \quad (16)$$

where h is layer thickness, η is free-surface elevation, and the angle brackets denote a spatial average over the domain. Note that in this paper, h and η are equivalent, although they would differ if bottom topography were included in the governing equations. Henceforth we use

thickness and free-surface elevation interchangeably.

In Fig. 9a, the energy continually increases because energy is continually injected but no energy is removed (except for the weak hyperviscosity). Therefore, no steady state exists in this case; the flow continually accelerates. Figures 9b and 9c, however, are approaching statistically equilibrated states where, on a time average, the forcing injects energy at the same rate that damping removes it.

Note that in all cases, the available potential energy exceeds the kinetic energy, by factors ranging from ~ 1.3 with strong damping (bottom panel) to ~ 5 with weak damping (top panel). For a fluid with a mean height H containing a characteristic height variation of ΔH , the available potential energy per area is $\sim g^2 \Delta H^2$ and the kinetic energy per area is $\sim g H U^2$. To order of magnitude, their ratio can be expressed as $E_{\text{APE}}/E_{\text{K}} \sim F^2/Ro^2 \sim L^2/L_d^2$, where $F = U/\sqrt{gH}$ and $Ro = U/2\Omega L$ are the Froude and Rossby numbers, respectively, U is a characteristic wind speed, L is a characteristic horizontal length scale of the flow, and we have used the fact that, in geostrophic balance, $fUL \sim g\Delta H$. In most of my simulations, $L/L_d > 1$, which explains why the available potential energies exceed the kinetic energies (Fig. 9).

FIG. 9.

It is interesting to characterize how the flow energy depends on the forcing and damping parameters. Although our convective parameterization has a strong physical motivation, it has the complexity that the increase in APE associated with the injection of a single mass pulse depends on the flow. Nevertheless, we can obtain an approximate expression for the rate of APE injection as follows. Suppose the original height field is h and an injected mass pulse produces a new height field of $h_{\text{new}} = h + \Delta h$. The change in APE caused by the injection of this pulse is

$$\Delta E_{\text{APE}} = \frac{g^2}{2} \int h_{\text{new}}^2 - \langle h_{\text{new}} \rangle^2 - h^2 + \langle h \rangle^2 dA, \quad (17)$$

which can be expressed as

$$\Delta E_{\text{APE}} = \frac{g^2}{2} \int \Delta h^2 - \langle \Delta h \rangle^2 dA + g^2 \int h \Delta h dA - g^2 \int \langle h \rangle \langle \Delta h \rangle dA \quad (18)$$

Because $\langle h \rangle$ and $\langle \Delta h \rangle$ are independent of latitude and longitude, the third integral equals $g^2 \langle h \rangle \langle \Delta h \rangle A$, where A is the area of the domain. In the second integral, Δh equals zero away from the storm, so the integral over the domain can be replaced with an integral over the storm location only. We will assume that h is constant across the storm (despite large h variations across the domain), which is approximately valid because the storm radius is much smaller than the typical length scale for height variations in the flow. This allows us to pull h out of the second integral. Noting that $\langle \Delta h \rangle \equiv A^{-1} \int \Delta h dA$, we can therefore write Eq. 18 as

$$\Delta E_{\text{APE}} = \frac{g^2}{2} \int \Delta h^2 - \langle \Delta h \rangle^2 dA + g^2 [h - \langle h \rangle] \langle \Delta h \rangle A \quad (19)$$

In the second term of Eq. 19, h is the original (pre-storm) height at the location of the injected storm. Although $h - \langle h \rangle$ is nonzero for any given storm, it averages to zero over many storms as long as the storms occur at random locations. The second term in Eq. 19 can therefore be approximated as zero.

In the absence of dynamics, the injected mass pulse alters the height field by an amount

$$g\Delta h = \pi^{1/2} \tau_{\text{storm}} s_{\text{max}} e^{-r^2/r_{\text{storm}}^2} \quad (20)$$

where r is the distance on the sphere as measured from the center of the injected storm. The change in mean height field caused by one storm is

$$g\langle \Delta h \rangle = \frac{\pi^{3/2} r_{\text{storm}}^2 s_{\text{max}} \tau_{\text{storm}}}{A} \quad (21)$$

where A is the area of the domain. Evaluating Eq. 19 using Eqs. 20–21, we obtain

$$\Delta E_{\text{APE}} = \frac{\pi^2}{2} \tau_{\text{storm}}^2 s_{\text{max}}^2 r_{\text{storm}}^2 \left[\frac{1}{2} - \frac{\pi r_{\text{storm}}^2}{A} \right] \quad (22)$$

Storms cover only a small fractional area of the domain; for the simulations presented here, $\pi r_{\text{storm}}^2/A \approx 0.002 - 0.0002$. The second term in square brackets can therefore be neglected. If we divide ΔE_{APE} by the mean time interval between storms, then we obtain the time-averaged rate at which storms increase the available potential energy of the fluid:

$$\left[\frac{dE_{\text{APE}}}{dt} \right]_{\text{storms}} = \frac{\pi^2 \tau_{\text{storm}}^2 s_{\text{max}}^2 r_{\text{storm}}^2}{4\tau_{\text{interval}}} \quad (23)$$

Analogously, we can determine the rate at which radiation *decreases* the available potential energy of the fluid. We can write this as

$$\left[\frac{dE_{\text{APE}}}{dt} \right]_{\text{rad}} = g^2 \int h \left[\frac{\partial h}{\partial t} \right]_{\text{rad}} - \langle h \rangle \left[\frac{\partial \langle h \rangle}{\partial t} \right]_{\text{rad}} dA \quad (24)$$

where the partial derivatives inside the integral give the contribution to the changes in h and $\langle h \rangle$ from radiation only. These are simply given by S_{rad} and $\langle S_{\text{rad}} \rangle$, respectively (see Eq. 6). Inserting the expression for S_{rad} into Eq. 24 and using the fact that h_{eq} is constant, we obtain finally

$$\left[\frac{dE_{\text{APE}}}{dt} \right]_{\text{rad}} = -\frac{E_{\text{APE}}}{\tau_{\text{APE}}} \quad (25)$$

Radiation therefore relaxes the APE toward zero over a timescale of τ_{APE} .

As illustrated in Fig. 9, the fluid can achieve an equilibrium where the rate of APE injection due to thunderstorms approximately balances the rate of APE loss due to radiation. This will lead to a constant time-averaged value of APE (around which short-term fluctuations in APE can occur on timescales of years or less). Setting the sum of Eqs. 23 and 25 to zero, we obtain the following prediction for the mean value of APE:

$$E_{\text{APE}} = \frac{\pi^2 \tau_{\text{storm}}^2 r_{\text{storm}}^2 s_{\text{max}}^2 \tau_{\text{APE}}}{4\tau_{\text{interval}}} \quad (26)$$

The APE predicted in Eq. 26 is an upper limit, and several processes suggest that the real value should be smaller by a factor of several. First, the height increase Δh predicted by Eq. 20 neglects fluid motion; in reality, the mass pulses expand by a factor of ~ 1.5 – 2 while they are injected, leading to values of Δh typically three times smaller than indicated in Eq. 20. The APE scales as $\Delta h^2 r_{\text{storm}}^2$, so, because of this effect, the APE injected per storm would be an order of magnitude smaller than in Eq. 26. (This effect is distinct from the

FIG. 10.

conversion of APE into KE associated with geostrophic adjustment.) Second, the advection of any large-scale flow across a mass pulse that is being injected smears the pulse out, again decreasing its height, increasing its area, and decreasing the APE increment associated with the pulse. (In these simulations, the location of a storm remains fixed throughout the storm lifetime, consistent with the assumption of no flow in the abyssal layer.) This effect becomes important for speeds fast enough to advect fluid across a storm diameter in less than a storm lifetime, which requires speeds exceeding $\sim 20 \text{ m sec}^{-1}$ for typical parameters ($r_{\text{storm}} = 2600 \text{ km}$ and $\tau_{\text{storm}} = 10^5 \text{ sec}$). Third, hyperviscosity could potentially play a role, although our simulations suggest that this effect is modest. A crude estimate of the time scale for hyperviscosity to damp the flow is $\nu_4^{-1} k^{-4}$, where ν_4 is the hyperviscosity coefficient and k is the dominant wavenumber of the flow. For typical parameters, this timescale is at least $0.5\text{--}1 \times 10^9 \text{ sec}$, suggesting that hyperviscosity plays a minor role in energy equilibration as long as $\tau_{\text{APE}} \leq 3 \times 10^8 \text{ sec}$. A comparison of Fig. 9a and 9b, which are identical except that τ_{APE} equals ∞ in Fig. 9a and 10^8 sec in Fig. 9b, confirms that hyperviscosity is a much weaker energy sink than radiation at the values of τ_{APE} considered here. Note that because the time-mean rate of interconversion between APE and kinetic energy sum to zero (see below), it is not appropriate in estimating the APE to include an APE sink associated with kinetic-energy production.

Despite these caveats, the above calculation predicts that the APE approximately scales as $\tau_{\text{storm}}^2 r_{\text{storm}}^2 s_{\text{max}}^2 \tau_{\text{APE}} / \tau_{\text{interval}}$, and my simulations support this prediction. Figure 10a depicts the equilibrated value of APE against this quantity, which we call the “energy parameter,” for a series of simulations with $s_{\text{max}} = 0.0033\text{--}3.33 \text{ m}^2 \text{ sec}^{-3}$, $\tau_{\text{APE}} = 10^7\text{--}10^8 \text{ sec}$, and mean $gh = 0.6 - 9 \times 10^5 \text{ m}^2 \text{ sec}^{-2}$. Intriguingly, the simulations follow the predicted scaling well, except that the mean APE values are on average ten times smaller than the upper limit in Eq. 26. The dash-dot line plots the energy parameter times 0.25 (whereas the predicted APE equals the energy parameter times 2.5). Despite the six-order-of-magnitude variation in the value of APE and the energy parameter for the different simulations, the actual energies all

fall within a factor of 3 of the dash-dot line. Figure 10b depicts the kinetic energy for these same simulations, with the same dash-dot line, which provides a reasonable fit here too.

Figure 10c depicts the equilibrated mass-weighted mean wind speed,

$$u_w = \sqrt{\frac{2E_K}{g\langle h \rangle A}} \quad (27)$$

which ranges from 0.4 to over 100 m sec⁻¹ for the simulations performed here (even higher values were achieved in simulations with $\tau_{\text{APE}} \rightarrow \infty$, which are not displayed in Fig. 10). Unlike APE and kinetic energy, there is no single functional relationship between the energy parameter and the mass-weighted speed. For a given total kinetic energy (whose approximate value is a function of the energy parameter), the mean wind speed *depends on the layer thickness* in addition to the energy parameter. This is illustrated by two simulations performed at an energy-parameter value of $8 \times 10^{23} \text{ m}^6 \text{ sec}^{-4}$ but different thicknesses (0.6 and $9 \times 10^5 \text{ m}^2 \text{ sec}^{-2}$); the kinetic energies differed by only a factor of 1.8 while the mass-weighted speeds differed by factors of 6 (see Fig. 10). Once a layer thickness (or deformation radius) is chosen, however, the speeds can be estimated from the energy parameter. In any given simulation, the maximum wind speed generally exceeds the mass-weighted mean speed by a factor of ~ 2 – 3 .

The kinetic energy cycle is subtle and interesting. Our governing momentum equation contains no sources or sinks; nevertheless, kinetic energy becomes approximately steady in time (Fig. 9, bottom two panels), indicating that creation and loss processes for kinetic energy reach an equilibrium. Gravitational (e.g., geostrophic) relaxation of the injected mass pulses converts APE into kinetic energy; this manifests as the winds associated with vortices, jets, and waves. On the other hand, the radiative relaxation acts as a kinetic-energy removal mechanism. To see how this operates, imagine an initially balanced flow that experiences radiative relaxation. The relaxation decreases the pressure-gradient forces, which then no longer fully balance the Coriolis forces. This unbalanced force component points *up-gradient*: toward pressure highs and away from pressure lows. A secondary circulation

therefore develops that drives fluid toward thick regions and away from thin regions. This converts kinetic energy into APE. Energetically, this conversion results from work performed by motion up the pressure gradient. Mechanically, the Coriolis acceleration produced by the secondary circulation opposes the balanced flow, thereby despinning it. In other words, a *thermally indirect* circulation develops that provides the dominant loss process for kinetic energy. This situation is alien to terrestrial-planet tropospheres, where the primary kinetic-energy loss mechanism is friction against the surface (Peixoto and Oort (1992), pp. 382-384). Nevertheless, it provides an elegant solution to the puzzle of how zonal jets on the giant planets equilibrate to finite speeds despite the continual forcing and presumably weak frictional drag (Showman and Ingersoll 1998).

In my simulations, thermally indirect circulations develop even in the absence of large-scale damping. The only requirement is the existence of an imbalance where Coriolis forces exceed pressure-gradient forces, which causes an unbalanced force component pointing up the pressure gradient. In the general case, such an imbalance results not only from radiative damping (which decreases the pressure gradients) but from the eddy-momentum convergences associated with the small-scale forcing (which accelerate the primary flow and therefore increase the Coriolis forces acting on that flow). Although damping is necessary for a forced flow to reach a quasi-equilibrium, it is not necessary for imbalance to occur: the continual jet acceleration can, by itself, generate such an imbalance. Thus, in all my simulations (regardless of whether damping is on or off), the Coriolis forces acting on the primary flow slightly exceed the pressure-gradient forces, leading to a thermally indirect secondary circulation that drives fluid from thin regions to thick regions. In the absence of damping, this up-gradient flow causes the height variations to increase over time. Figures 1 and 4 clearly demonstrate that such increases indeed occur when $\tau_{\text{APE}} \rightarrow \infty$.

Interestingly, the flow in Fig. 8a appears to equilibrate during the last ~ 7 years, particularly in kinetic energy, despite the continual forcing and absence of large-scale damping. The flattening in total energy probably results partly from hyperviscosity and, more

importantly, from the fact that the energy injection rate is not constant over time even though storm parameters τ_{storm} , τ_{interval} , s_{max} and r_{storm} are held constant throughout the simulation. Recall that advection of large-scale flow across a mass pulse smears the pulse out while it is being injected. Because the flow speeds increase over time in Fig. 8a, the degree of smearing of injected mass pulses increases over time too, and the rate of energy injection decreases over time. By the end of the simulation, the flow speeds in Fig. 8a exceed that necessary for substantial smearing of injected pulses over almost half of the domain. This suggests that the rate of energy injection decreases by a factor of ~ 2 throughout the simulation. It is particularly notable that kinetic energy seems to flatten faster than APE. A simple scaling argument can explain this fact. As the jets and vortices widen over time (cf Fig. 1), L/L_d increases, where L is the characteristic width of jets and vortices. Thus, the ratio of kinetic energy to APE, which is approximately L_d^2/L^2 , decreases over time. Therefore, even if APE increased linearly in time, we would expect that kinetic energy would *not* increase linearly — instead, the rate of increase would fall off, as observed in Fig. 8a.

FIG. 11.

b. Effect of damping and forcing on the physical-space evolution

My simulations show that, for given forcing parameters, the preferred length scale of the jets and vortices decreases as τ_{APE} is decreased. This result agrees qualitatively with analogous results for purely two-dimensional turbulence (Danilov and Gurarie 2001, 2002; Marcus et al. 2000) but has not previously been documented in the forced-dissipative shallow-water system. Figure 11 shows the spatial structure of layer thickness and winds for simulations with $\tau_{\text{APE}} = \infty$ (top), 10^8 sec (middle) and 10^7 sec (bottom) after approximately 8400 Earth days (more than 20,000 Jupiter rotations) of evolution. The top frame, in which damping has been turned off, represents a snapshot of a continually accelerating flow. The evolution has proceeded far enough for the midlatitudes to become dominated by a single, large anticyclone, which sweeps up the smaller anticyclones that are continually produced by the forcing. Unlike the top panel, however, we emphasize that the bottom two panels depict

statistically *equilibrated* states rather than transient stages of an accelerating flow. In these cases, the radiative damping removes the injected small-scale energy before it has time to cascade up to the largest scales, which leads to an equilibrated state with coherent structures much smaller than the domain size. In the snapshot with $\tau_{\text{APE}} \rightarrow \infty$, coherent structures reach $\sim 20\text{--}40^\circ$ in size. With damping, however, vortices are smaller: about $15\text{--}20^\circ$ and $\sim 8\text{--}10^\circ$ when τ_{APE} is 10^8 and 10^7 sec, respectively. These and other simulations suggest that ten-fold changes in damping cause 1.5-to-2-fold changes in the size of coherent structures. This implies that the size of coherent structures scales as τ_{APE}^γ , with $\gamma \sim 0.2\text{--}0.3$.

The fact that coherent structure widths in my simulations scale as $\tau_{\text{APE}}^{0.2\text{--}0.3}$ agrees with previous studies. In the two-dimensional barotropic system, which has infinite deformation radius, turbulence studies of zonal jets forced at small scales and damped with a linear drag predict that the peak energy resides at an inverse wavenumber $\beta^{-1/2}\epsilon^{1/4}\tau^{1/4}$, where ϵ is the energy-injection rate and τ is the drag time scale (Danilov and Gurarie 2002; Marcus et al. 2000; Sukoriansky et al. 2007). A weakly nonlinear investigation of the same phenomenon predicts that the meridional jet separation scales as $\tau^{1/3}$ (Manfroi and Young 1999). In the quasigeostrophic system, when the flow length scales far exceed the deformation radius, the energy peaks at an inverse wavenumber $\sim L_d^{3/4}\tau^{3/8}\epsilon^{1/8}$ (Smith et al. 2002), where here τ is the time constant for relaxation of pv (which acts primarily as an APE damping at large scales). The range of damping exponents predicted in these studies, 0.25–0.38, approximately matches that seen in my simulations, suggesting that the scalings, while not rigorous in the context of shallow-water, nevertheless have relevance. [Note that a different scaling regime occurs when damping is strong enough that the turbulence is affected by neither β nor the deformation radius. In this case, scaling arguments predict vortex sizes of $\sim 0.05\epsilon^{1/2}\tau^{3/2}$ (Danilov and Gurarie 2001; Marcus et al. 2000; Smith et al. 2002); however, this regime is not relevant to the simulations presented in Fig. 11.]

Next consider the influence of forcing. My simulations at small deformation radius indicate that the confinement of jets to equatorial regions (with vortex domination in

midlatitudes) holds over a wide range of forcing amplitude. Figure 12 illustrates this behavior for simulations with s_{\max} values of 0.333, 0.1, 0.0333, and 0.00333 $\text{m}^2 \text{sec}^{-3}$ from top to bottom, respectively, at about 6800 Earth days; τ_{APE} is held constant at 10^8 sec in all four simulations. Despite the fact that the energy-injection rate varies by six orders of magnitude from top to bottom, and the peak wind speeds vary by over two orders of magnitude, the flow fields are qualitatively similar in all cases. Furthermore, I find that the coherent structure size decreases with decreasing s_{\max} when other parameters are held constant, in qualitative agreement with published scalings. However, there is quantitative disagreement. As described earlier, barotropic studies of zonal jets forced at small scales and damped at large scales predict that the jet separation scales as $\epsilon^{1/4}$, whereas quasigeostrophic studies of isotropic turbulence at scales exceeding the deformation radius predict that vortex size scales as $\epsilon^{1/8}$. For the six-order-of-magnitude variation in energy-injection rate in Fig. 12, these scalings predict that barotropic jet separations and vortex sizes should vary by factors of ~ 30 and 6, respectively; in contrast, the actual length scales L in my simulations vary by only a factor of $\sim 2\text{--}3$ over this range of energy-injection rate (Fig. 12). This disagreement probably occurs because the scalings assume that the length scale of peak energy, L , far exceeds the forcing length scale L_{force} ; however, this condition is violated in the lower two panels of Fig. 12, where the vortex size only modestly exceeds the forcing scale $L_{\text{force}} \sim 2r_{\text{storm}} \sim 4^\circ$. As forcing is turned down and L approaches L_{force} , one expects that L should become constant with further decreases in the forcing, in qualitative agreement with my simulations (compare the bottom two panels in Fig. 12). Furthermore, the equatorial jet probably cannot become narrower than the equatorial waveguide, suggesting that the equatorial jet width should also become constant in the limit that the forcing amplitude tends towards zero.

FIG. 12.

It is interesting to compare the behavior of simulations with strong forcing/strong damping and weak forcing/weak damping at approximately constant total energy. Fig. 11 (bottom) and Fig. 12 (second panel) present these limits. These two simulations have essentially identical energy parameters, and have total energies differing by less than a factor

of two, but the energy-injection rate and damping rate are ten times stronger in Fig. 11 (bottom) than in Fig. 12 (second panel). These simulations suggest that, at constant total energy, the sizes of midlatitudes vortices increase as forcing and damping strengths decrease. This result agrees qualitatively with the quasigeostrophic scaling $L \sim L_d^{3/4} \tau^{3/8} \epsilon^{1/8}$ at scales exceeding the deformation radius (Smith et al. 2002): The total energy per mass E in this system is $\epsilon\tau/2$ (Smith 2004), implying that $L \sim L_d^{3/4} E^{1/8} \tau^{1/4}$. At constant energy, a ten-fold increase in τ_{APE} should therefore cause nearly a two-fold increase in L . The fact that midlatitude vortices in Fig. 11 (bottom) are roughly $\sim 8\text{--}10^\circ$ across, while those in Fig. 12 (second panel) reach $\sim 10\text{--}20^\circ$ in diameter, roughly matches this prediction.

In the cases shown above (Figs. 11–12), the *qualitative* behavior — namely, the dominance of vortices over jets in midlatitudes — holds at any value of τ_{APE} and s_{max} . This makes sense, because the absence of mid-latitude jets results not predominantly from the forcing or damping but from the suppression of the Rhines effect by the small deformation radius, which is approximately the same for all three simulations in Fig. 11.

FIG. 13.

Nevertheless, strong damping can prevent the development of zonally elongated structures when they would otherwise occur (Fig. 13). As described previously, simulations with midlatitude $L_d \sim 5000$ km and weak damping produce a banded structure with alternating zonal jets. Figure 13 depict two simulations that are identical except that τ_{APE} equals 10^8 sec in the top panel and 10^7 sec in the bottom panel. A strong equatorial jet forms in both cases. However, the figure demonstrates that, when the forcing is strong enough, the *midlatitude* flow is no longer zonal but develops midlatitude vortices at the expense of the midlatitude jets. This result is consistent with purely two-dimensional studies showing that strong friction can prevent the production of zonal jets by removing injected small-scale energy before it cascades up to the Rhines scale (Danilov and Gurarie 2002; Marcus et al. 2000; Smith et al. 2002; Vasavada and Showman 2005). This jet-inhibition mechanism is distinct from that described earlier (wherein a small deformation radius suppresses the Rhines effect). Thus, at least two distinct mechanisms exist in the forced shallow-water system for

inhibiting jets despite the presence of β .

A comparison of the top panel of Fig. 11 and the bottom panel of Fig. 1 indicates that neither resolution nor the details of the forcing parameters affect the qualitative results presented in this paper. The simulation in Fig. 1 adopted a resolution of 512×298 and used a storm radius of only 0.7° ; in contrast, Fig. 11 had a resolution of 256×149 and used larger storms (radius of 2.1°) that were injected 8 times less often. Although the resolutions, storm sizes, and energy injection rates differed between these cases, both simulations produced qualitatively identical end states, consisting of a single large anticyclone in midlatitudes and two broad equatorial jets equatorward of $\sim 30^\circ$ latitude.

c. Effect of injecting storms only in cyclonic regions

On Jupiter, thunderstorms are observed to occur primarily in the cyclonic bands (called belts) and at westward jets; comparatively few thunderstorms occur in the anticyclonic bands (called zones) (Little et al. 1999; Porco et al. 2003). To investigate this phenomenon, I performed a series of simulations, which I dub the CR simulations, where thunderstorms were injected at random locations, as before, but only in cyclonic regions. (Whenever a randomly chosen trial storm location corresponded to an anticyclonic region, that selection was discarded and another random location was picked until it corresponded to a cyclonic region.) The mass pulses were positive. These simulations generally adopted midlatitude deformation radii of ~ 1200 km, $\tau_{\text{APE}} \rightarrow \infty$ and s_{max} ranging from $0.033\text{--}1$ m² sec⁻³.

In most cases, these CR simulations produced wide equatorial jets with speeds only slightly less than those in identical simulations with my standard forcing. This comparison suggests that the processes that pump the equatorial jet are not strongly affected by the change in forcing. This makes sense, because the equatorial band has cyclonic relative vorticity in all my simulations (e.g., Figs. 1–2, 4–5, 11, 12, and 13). Therefore, storms occur randomly throughout the equatorial band — and can pump eddy momentum up-gradient into the retrograde jet — regardless of whether standard or CR forcing is adopted.

However, in the midlatitudes, the CR simulations generally lacked vortices and jets, produced only weak flow velocities, and had minimal height variability in the longitudinal direction (in contrast to the behavior in identical simulations with standard forcing, where the midlatitudes became dominated by strong vortices with order-unity thickness variations in longitude). This behavior presumably occurred because cyclonic regions are thinner than anticyclonic regions, so the CR forcing naturally removes variability in the layer thickness. Injecting storms into the cyclonic regions also inhibits the formation of vortices because the injected mass pulses attempt to adjust into anticyclones, which tend to be unstable in cyclonic shear zones (Marcus 1990; Marcus et al. 2000).

The lack of midlatitude vortices and jets in my CR simulations contrasts with the results of Li et al. (2006), who performed one-layer quasigeostrophic simulations on a β plane. To force the flow, they injected isolated mass pulses at the locations of minimum layer thickness, which generally have cyclonic relative vorticity. Therefore, their forcing is analogous to my CR forcing. In contrast to my finding that CR simulations develop featureless midlatitude flows, however, Li et al. (2006) reported the development of strong zonal jets and vortices.

The explanation for this discrepancy is unclear, but may involve the rate of forcing. As described earlier, eddy forcing induces a thermally indirect circulation that pumps fluid up-gradient from thin regions to thick regions. CR forcing counteracts this effect by placing storm mass preferentially in thin regions. Thus, in CR-type forcing, one expects that strong vortices and/or jets can only exist if the timescale for the indirect circulation to increase the fluid's height variability is shorter than the timescale for the CR forcing to decrease it. The former timescale is roughly $\tau_{\text{indirect}} \sim L/\bar{v}$, and the latter is $\tau_{\text{fill}} \sim \langle gh \rangle A \tau_{\text{interval}} / (r_{\text{storm}}^2 s_{\text{max}} \tau_{\text{storm}})$. The key question is how the indirect-circulation flow speed \bar{v} depends on the storm parameters s_{max} , τ_{storm} , and τ_{interval} , which is unclear. The storms in Li et al. (2006)'s simulation have equivalent values of s_{max} comparable to mine (e.g., their Fig. 3c implies that storms locally increase the fluid thickness by $\sim 3 \times 10^4 \text{ m}^2 \text{ sec}^{-2}$, which is similar to that in my Figs. 1–2 and 4–5). On the other hand, they introduced the storms much less frequently (typical

$\tau_{\text{interval}} \sim 50$ days according to their Fig. 3f, in comparison to $\tau_{\text{interval}} \sim 1$ day here). It appears that my CR simulations are in a regime where, in the midlatitudes, the CR forcing removes the height variability faster than the indirect circulation produces it. I speculate that Li et al. (2006)'s simulations may be in the reverse regime where the indirect circulation creates height variability faster than the CR injection removes it, hence allowing the development of large height variations and the fast winds that accompany them. Further exploration of these possibilities is deferred to future work.

5. Cyclone-anticyclone asymmetry

Unlike the standard quasigeostrophic equations, the shallow-water equations can exhibit an asymmetry between cyclones and anticyclones. Decaying shallow-water simulations initialized with equal-strength cyclones and anticyclones show that, as the flow evolves, the anticyclones become stronger and more compact than the cyclones (Arai and Yamagata 1994; Cho and Polvani 1996b; Polvani et al. 1994; Stegner and Dritschel 2000). In decaying turbulence simulations initialized with zero skewness, the asymmetry only develops when $F^2/Ro > 0.13$, where $F = U/\sqrt{gh}$ and $Ro = U/2\Omega L$ are the Froude and Rossby numbers, respectively, and L is a characteristic horizontal length scale of the flow (Cho and Polvani 1996b; Iacono et al. 1999a). In geostrophic balance, the ratio F^2/Ro is just the fractional height variation associated with the flow, so this criterion is equivalent to stating that fractional height variations must exceed $\sim 13\%$ for an asymmetry to develop. FIG. 14.

In my experiments, the cyclone-anticyclone asymmetry may be influenced not only by the inherent asymmetry of the dynamical equations but also by the asymmetry of the forcing. In particular, the standard forcing involves the injection of positive mass pulses, which geostrophically adjust into anticyclones (Figs. 1 and 4). It is therefore of interest to determine whether an asymmetry develops, how it depends on the forcing, and whether it follows the criterion identified in the decaying simulations.

The cyclone-anticyclone asymmetry can be quantified by calculating the vorticity

skewness, defined as

$$Sk = \frac{\langle \zeta^3 \rangle}{\langle \zeta^2 \rangle^{3/2}} \quad (28)$$

where ζ is the relative vorticity and angle brackets denote the spatial average over the domain. Note that because our standard domain resides only in one hemisphere, we need not multiply Eq. 28 by the sign of latitude, as is commonly done for a full sphere (Iacono et al. 1999a).

My simulations with standard forcing generally develop negative skewness, indicating a preference for anticyclones over cyclones. The solid curves in Fig. 14 illustrate this effect for simulations with midlatitude deformation radii of 1200 km, 3000 km, and 5000 km from top to bottom, respectively. As the first few mass pulses are injected, causing formation of isolated anticyclones (e.g., see Figs. 1 and 4), the skewness reaches -3 or less at early times. Once the continued forcing causes turbulence to fill the entire domain, however, the skewness generally stabilizes at negative values between 0 and -1 , although in some simulations it reaches -2 . In Fig. 14, $F^2/R \sim 1, 0.4$, and 0.09 in the top to bottom panels, respectively. Interestingly, even in simulations with F^2/R as low as 0.02 , the skewness remains negative (with typical values of -0.5), suggesting that the asymmetry in such cases is imposed by the forcing rather than by an inherent difference in stability between cyclones and anticyclones.

To investigate the effect of forcing on the asymmetry, I reran several cases with the injection of *negative* mass pulses ($s_{\max} < 0$), leading to the production of numerous small cyclones rather than anticyclones. Fig. 14 depicts three such cases, in dotted lines, for midlatitude deformation radii of ~ 1200 km, 3000 km, and 5000 km from top to bottom, respectively. The skewness rapidly becomes large ($Sk > 1$) during the first ~ 100 days of the simulation as isolated cyclones form. Once turbulence fills the domain, the skewness stabilizes at values that exceed by 0.5 – 1 the corresponding skewness values for simulations with positive mass forcing. This proves that the type of forcing can substantially affect the value of Sk for a given F^2/R . Nevertheless, even with the injection of negative mass pulses (which become cyclones), the fluid exhibits a preference for anticyclones in cases with large F^2/R . This is illustrated by the slightly negative time-averaged values of Sk at late times in Figs. 14b

(dotted line).

6. Comparison with Jupiter and Saturn

The simulations here share both similarities and differences with the giant planets. The most glaring discrepancy involves the jet/vortex distribution. On Jupiter and Saturn, the dominant flow consists of zonal jets to very high latitudes. Jupiter's banded cloud structure extends to $\sim 50^\circ$ latitude, and although regions poleward of 60° lack the banded cloud pattern and contain numerous vortices, careful observations show unmistakable jets even at latitudes of $\sim 85^\circ$ (Porco et al. 2003). On Saturn, even the zonally banded cloud structure extends to latitudes of 85° (Vasavada et al. 2006). Where they exist, the zonal cloud bands are remarkably uniform in the zonal direction, suggesting minimal meandering of the jets in longitude despite the presence of numerous small vortices. In contrast, at deformation radii comparable to those estimated for Jupiter (1000–2000 km), the midlatitude flow in my simulations becomes dominated by strong vortices with no regular jet pattern at all. This discrepancy suggests either that the actual deformation radius is larger than previously believed or that three-dimensional effects, not included in the shallow-water equations, alter the dynamics in a fundamental manner.

The most plausible reconciliation of the observed dominance of jets on Jupiter with the small inferred deformation radius is that baroclinic turbulence in the cloud layer drives a *barotropic* zonal flow, which would have an effectively infinite deformation radius. (Recall that the deformation radius in the reduced-gravity shallow-water system, and existing estimates of L_d for Jupiter (Cho et al. 2001; Marcus 1988), correspond to *internal* deformation radii associated with baroclinic flow in a statically stable cloud layer.) Because of its infinite deformation radius, a barotropic mode would presumably follow two-dimensional dynamics and would therefore favor jets over vortices, helping to explain the observations. Two-layer quasigeostrophic models in which baroclinic turbulence drives a barotropic zonal flow have been explored by Williams (1979), Panetta (1993), and Young and Thompson (2006). In these

cases, however, the layers involving the barotropic mode are the same as the layers in which the baroclinic turbulence occurs (the baroclinic turbulence manifests as perturbations in the interface between the two layers). For the giant planets, a barotropic mode must presumably penetrate orders of magnitude deeper in pressure and depth than the base of the baroclinic zone (Vasavada and Showman 2005); the key question is whether a barotropic mode can develop in this case. Recent analytical (Showman et al. 2006) and numerical (Lian et al. 2006) models show that idealized shallow jet forcing confined to the cloud layer can indeed drive a deep barotropic flow that extends far below the base of the baroclinic zone. It remains to be seen whether full turbulence in the baroclinic cloud zone can drive barotropic zonal jets, however; this is an important avenue for future research.

In most of my simulations, a near-cancellation develops between the eddy-momentum convergence, $-(a \cos^2 \phi)^{-1} \partial(\overline{u'v'} \cos^2 \phi)/\partial\phi$, and the Coriolis acceleration on the mean-meridional flow, $f\bar{v}$. Several authors have suggested that just such a balance between the eddy-momentum convergence and $f\bar{v}$ occurs at the cloud level on Jupiter and Saturn (Del Genio et al. 2007; Showman et al. 2006). If the eddy-momentum convergence correlates with the jet pattern, this balance would require equatorward flow across eastward jets and poleward flow across westward jets, which in turn would imply that, below the clouds, ascending motion occurs in cyclonic regions (belts) and descending motion occurs in anticyclonic regions (zones). This inference is consistent with recent observations that thunderstorms, which presumably correspond to ascending motion, occur primarily in the belts (Ingersoll et al. 2000; Little et al. 1999; Porco et al. 2003). A near-cancellation of the eddy-momentum convergence and $f\bar{v}$ would also explain the dual observations that eddies pump momentum into the jets (Del Genio et al. 2007; Ingersoll et al. 1981; Salyk et al. 2006) and that the observed jet speeds are nearly constant in time.

Does evidence exist that thunderstorms participate in an inverse cascade on Jupiter and Saturn? Thunderstorms only rarely lead to the creation of long-lived anticyclonic vortices; Porco et al. (2005) show a possible example for Saturn. More commonly, a bright anvil

cloud expands over $\sim 1\text{--}3$ days and then shears apart without leaving a residual vortex. However, vortex formation is probably not the dominant mechanism by which thunderstorms can affect the flow. Expanding thunderstorms could potentially cause an up-gradient $\overline{u'v'}$ momentum flux into zonal jets even if the thunderstorms themselves shear apart and do not form long-lived vortices. This type of behavior has long been known in barotropic numerical simulations (Huang and Robinson 1998; Nozawa and Yoden 1997): the eddies introduced by small-scale forcing can directly accelerate the jets (an interaction which is nonlocal in spectral space) without forming vortices and undergoing an intermediate set of vortex mergers. And exactly the same process occurs in my simulations — for example, thunderstorms injected near the equator shear apart without forming vortices, yet in so doing they accelerate the equatorial jets. The observed small-scale eddy pumping of jets on Jupiter and Saturn (Del Genio et al. 2007; Salyk et al. 2006) provides evidence for this type of spectrally non-local inverse cascade, although it remains unclear whether the eddies that cause this pumping result from thunderstorms or other processes (Del Genio et al. 2007).

Can my simulations explain the mean wind speeds on Jupiter? To answer this question, we must estimate the likely values of the forcing and damping parameters. Several authors have suggested, in analogy with Earth's tropics, that Jovian thunderstorms can transport most of the heat flux through the cloud layer (Banfield et al. 1998; Gierasch et al. 2000). If so, then the globally averaged thunderstorm mass flux is $\dot{M} \sim F/(c_p \Delta\theta)$, where F is the heat flux, c_p is specific heat, and $\Delta\theta$ is the static stability across the layer (or equivalently, the mean temperature difference between updrafts and the subsiding environmental air). The characteristic overturn time for the cloud layer is then $\sim pc_p \Delta\theta/(g_{\text{real}} F)$, where p is the pressure of the layer and $g_{\text{real}} = 23 \text{ m sec}^{-2}$ is the actual (not reduced) gravity. Equating this to the mean overturn time of the shallow-water layer in my simulations, $\sim \langle gh \rangle A \tau_{\text{interval}} / (\pi^{3/2} \tau_{\text{storm}} r_{\text{storm}}^2 s_{\text{max}})$, we find that the value of s_{max} needed to transport Jupiter's total heat flux is

$$s_{\text{max}} = \frac{\langle gh \rangle A \tau_{\text{interval}} g_{\text{real}} F}{\pi^{3/2} \tau_{\text{storm}} r_{\text{storm}}^2 p c_p \Delta\theta} \quad (29)$$

The shallow-water layer represents the statically stable troposphere above the water-condensation region at $\sim 5\text{--}10$ bars, so we expect $p \sim 10$ bars. Static stability associated with condensation of three-times solar water would imply $\Delta\theta \sim 10$ K, which is also consistent with the expected deformation radius. Other expected values are $F \sim 8 \text{ W m}^{-2}$ for Jupiter and $c_p = 1.3 \times 10^4 \text{ J kg}^{-1} \text{ K}^{-1}$. To transport Jupiter's heat flux under storm parameters typical for my simulations ($\tau_{\text{interval}} = 10^5 \text{ sec}$, $\tau_{\text{storm}} = 10^5 \text{ sec}$, $r_{\text{storm}} = 2600 \text{ km}$, $gh \sim 6 \times 10^4 \text{ m}^2 \text{ sec}^{-2}$, and $A = 1.0 \times 10^{16} \text{ m}^2$), we must therefore have $s_{\text{max}} = 0.03 \text{ m}^2 \text{ sec}^{-3}$. The uncertainty is probably a factor of ~ 3 , primarily because of the uncertainty in p and $\Delta\theta$. With regard to damping, we expect that the time to radiatively remove the lateral temperature differences, τ_{APE} , is equivalent to the time to radiatively relax the temperature toward zero, $\sim pc_p T / (g_{\text{real}} F)$, where T is the mean temperature. [Note that the time to cool air by a potential temperature $\Delta\theta$, $\sim pc_p \Delta\theta / (g_{\text{real}} F)$, is not an appropriate estimate for τ_{APE} .] Realistic radiative calculations for the emission level (~ 0.3 bar) predict radiative time constants of $\sim 1.3 \times 10^8 \text{ sec}$ on Jupiter (Conrath et al. 1990); the crude formula above gives values in approximate agreement. However, we are interested in the radiative time constant for the layer extending to ~ 10 bars, and in this case the time constant has a larger value $\tau_{\text{APE}} \sim 0.3 - 1 \times 10^{10} \text{ sec}$. Feedbacks wherein albedo or latent heating differ between hot and cold regions could potentially complicate this picture.

Combining these estimates, my simulations indeed predict speeds that, to order-of-magnitude, agree with observed wind speeds on Jupiter. The probable value of the energy parameter $\tau_{\text{storm}}^2 r_{\text{storm}}^2 s_{\text{max}}^2 \tau_{\text{APE}} / \tau_{\text{interval}}$ is $\sim 10^{25} \text{ m}^6 \text{ sec}^{-4}$, with a probable uncertainty of an order of magnitude. With this value, Fig. 10c predicts a best-guess mass-weighted mean speed of $\sim 40 \text{ m sec}^{-1}$, with an allowed range of $\sim 10\text{--}80 \text{ m sec}^{-1}$ when the uncertainties are considered. These values are similar to the mean speed of Jupiter's jets, $\sim 30\text{--}40 \text{ m sec}^{-1}$ (Vasavada and Showman 2005). This crude agreement suggests that the energy cycle in my simulations could have relevance to the giant planets. Interestingly, thermally indirect meridional circulations have been inferred in the upper tropospheres and lower stratospheres

of all four giant planets (Conrath et al. 1990; Gierasch et al. 1986). Nevertheless, in my simulations where thunderstorms were injected primarily in cyclonic regions (as observed on Jupiter), the simulations developed strong equatorial jets but only weak midlatitude flow.

The predominance of anticyclones in the simulations agrees with Jupiter, where 90% of compact vortices are anticyclonic (Li et al. 2004; Mac Low and Ingersoll 1986). And the elongation of vortices at sizes exceeding a few thousand km agrees with Jupiter and Saturn, where similar elongation is observed (Mac Low and Ingersoll 1986; Vasavada et al. 2006).

The simulations that produce realistic (Jovian) wind speeds at realistic deformation radii develop order-unity height variations, which suggests that ageostrophic effects are important despite the essentially balanced nature of the large-scale flow. On Jupiter, such thickness variations would correspond to order-unity pressure variations on isentropes in the weather layer. Such large-amplitude isentrope variations have been proposed observationally and theoretically (Allison 2000; Allison et al. 1995; Gierasch 2004; Showman and Dowling 2000; Showman and Ingersoll 1998).

Finally, we provide a comparison of large anticyclones on Jupiter and in the simulations. Recent cloud-tracking analysis of high-resolution Galileo images of Jupiter's Great Red Spot demonstrate that a thin ring of cyclonic vorticity surrounds the main anticyclone (Choi et al. 2005). My simulations produce just such features, as shown in Fig. 15. One possible mechanism is that expansion of an anticyclone during vortex mergers causes horizontal convergence in the fluid surrounding the anticyclone, which would impart cyclonic vorticity to this fluid as it spins up to conserve potential vorticity. However, not all anticyclones in the simulations grow rapidly. Another mechanism is that vortex interactions (e.g., close encounters) strip material from the outer edge of an anticyclone, ensuring that the vortex wind speeds drop rapidly to zero outside the vortex; this high shear would manifest as a ring of cyclonic vorticity. Future work is needed to investigate these and other mechanisms and to determine what sets the width and amplitude of this feature for the Great Red Spot.

FIG. 15.

7. Conclusions

This paper presented numerical simulations of the forced-dissipative shallow-water equations intended to test the hypothesis that moist convection (thunderstorms) can drive the cloud-level flow observed on Jupiter and Saturn. The simulations showed that a small deformation radius similar to that expected in the cloud layers of Jupiter and Saturn ($\sim 1000\text{--}2000$ km) suppresses the Rhines effect, leading to a field of vortices rather than zonal jets. Because the deformation radius increases toward the equator, a critical latitude exists below which the flow produces jets and above which it produces vortices. This result agrees with quasigeostrophic studies (Okuno and Masuda 2003; Smith 2004; Theiss 2004) but has not previously been demonstrated in the full shallow-water system. The fact that zonal jets dominate the circulation on Jupiter and Saturn up to high latitudes suggests either that the deformation radius is much greater than previously believed or that the one-layer shallow-water system contains insufficient physics to describe the cloud-layer flows on giant planets. To produce a jet-dominated (rather than vortex-dominated) flow, the midlatitude deformation radius would have to be at least 5000 km, which seems unlikely based on observational and theoretical constraints on L_d . Instead, it seems more likely that *baroclinic* turbulence (associated with the 1000–2000 km deformation radius) drives a *barotropic* flow, whose dynamics would naturally become jet- rather than vortex-dominated. A multi-layer model is needed to address these issues.

My results show that the forcing and damping parameters can have a strong influence on the flow structure. When damping is turned off, the inverse cascade proceeds unhindered, leading to vortices and jets that widen continually over time until approaching the domain size. Strong damping can remove energy before it has time to cascade upscale, however, leading to small jets and vortices in the equilibrated state. My simulations suggest that ten-fold changes in the damping strength cause approximately 1.5-to-2-fold changes in the size of coherent structures. Furthermore, I find — even when zonally elongated structures (jets) would occur under conditions of *weak* damping — that *strong* damping can prevent the formation of these

structures. In this case, the damping removes the energy before it reaches the Rhines scale, leading to the production of quasi-isotropic vortices rather than jets. This result extends to the shallow-water system analogous behavior that has been observed in barotropic turbulence with a β effect (Danilov and Gurarie 2002; Marcus et al. 2000). Because the turbulence is strongly latitude-dependent, the forcing/damping parameter values where these transitions occur depend on latitude.

Thus, these simulations have identified *two* mechanisms by which jet production can be inhibited in shallow-water turbulence — having a small deformation radius, which suppresses the Rhines effect; or having strong damping, which prevents the energy from reaching sufficiently large scales to be dominated by β .

The numerical simulations described here possess an interesting energy cycle that may be relevant for Jupiter and Saturn. Both the small-scale forcing (injection of sporadic, isolated circular mass pulses representing moist convection) and the large-scale damping (radiation) affect the available potential energy but not (directly) the kinetic energy. (No frictional drag was included in the equations, since the giant planets possess no solid surfaces.) Once a statistical equilibrium is reached, the forcing adds APE at the same rate that damping removes it. Geostrophic adjustment convert APE into kinetic energy, but the radiative damping drives a thermally indirect secondary circulation that despins the fluid, converting kinetic energy back into APE at the same rate. Thus, the steady state that develops is one where the primary kinetic-energy loss mechanism is thermally indirect circulations rather than friction. On the giant planets, it is possible that three-dimensional effects (wave breaking, Kelvin-Helmholtz instabilities) acting on the large-scale flow could act as a weak frictional drag. However, thermally indirect circulations have been observed in the upper tropospheres of all four giant planets (Conrath et al. 1990; Gierasch et al. 1986), and it is also possible that such circulations provide the dominant kinetic-energy sink.

For forcing and damping parameters relevant to Jupiter, the simulations produce mean speeds of $\sim 40 \text{ m sec}^{-1}$ and peak speeds of $> 100 \text{ m sec}^{-1}$, similar to the observed speeds

on Jupiter. This supports the idea that the simulations have captured some of the key energy production and loss processes occurring in the cloud layers of giant planets.

Acknowledgment. I thank Peter Gierasch for hosting me at Cornell during several summer visits, Tim Dowling for discussions about EPIC, B. Galperin and J. Theiss for discussions about fluid mechanics, and Tony Del Genio and two anonymous referees for helpful reviews. This research was supported by NSF Planetary Astronomy grant AST-0206269 and NASA Planetary Atmospheres grant NNG06GF28G.

REFERENCES

- Achterberg, R. K., and A. P. Ingersoll, 1989: A normal-mode approach to Jovian atmospheric dynamic. *Journal of Atmospheric Sciences*, **46**, 2448–2462.
- Allison, M., 2000: A similarity model for the windy jovian thermocline. *Planet. Space Sci.*, **48**, 753–774.
- Allison, M., A. D. Del Genio, and W. Zhou, 1995: Richardson number constraints for the Jupiter and outer planet wind regime. *Geophys. Res. Lett.*, **22**, 2957–2960.
- Arai, M., and T. Yamagata, 1994: Asymmetric evolution of eddies in rotating shallow water. *Chaos*, **4**, 163–175.
- Banfield, D., P. J. Gierasch, M. Bell, E. Ustinov, A. P. Ingersoll, A. R. Vasavada, R. A. West, and M. J. S. Belton, 1998: Jupiter's Cloud Structure from Galileo Imaging Data. *Icarus*, **135**, 230–250.
- Cho, J. Y.-K., and L. M. Polvani, 1996a: The morphogenesis of bands and zonal winds in the atmospheres on the giant outer planets. *Science*, **8**(1), 1–12.
- Cho, J. Y.-K., and L. M. Polvani, 1996b: The emergence of jets and vortices in freely evolving, shallow-water turbulence on a sphere. *Physics of Fluids*, **8**, 1531–1552.
- Cho, J. Y.-K., M. de la Torre Juárez, A. P. Ingersoll, and D. G. Dritschel, 2001: A high-resolution, three-dimensional model of Jupiter's Great Red Spot. *J. Geophys. Res.*, **106**, 5099–5106.
- Choi, D. S., P. J. Gierasch, D. Banfield, and A. P. Showman, 2005: Velocity and vorticity measurements of Jupiter's Great Red Spot using automated cloud feature trackers. *Eos Trans. AGU*, Fall Meeting Supplement, **86**(52), P11A–0089.
- Conrath, B. J., P. J. Gierasch, and S. S. Leroy, 1990: Temperature and circulation in the stratosphere of the outer planets. *Icarus*, **83**, 255–281.

- Danilov, S., and D. Gurarie, 2001: Forced two-dimensional turbulence in spectral and physical space. *Phys. Rev. E*, **63**(6), 061,208–1 – 061,208–12.
- Danilov, S., and D. Gurarie, 2002: Rhines scale and spectra of the β -plane turbulence with bottom drag. *Phys. Rev. E*, **65**(6), 067,301–+.
- Del Genio, A. D., J. M. Barbara, J. Ferrier, A. P. Ingersoll, R. A. West, A. R. Vasavada, J. Spitale, and C. C. Porco, 2007: Saturn eddy momentum fluxes and convection: first estimates from Cassini images. *Icarus*, submitted.
- Dowling, T. E., 1995: Dynamics of jovian atmospheres. *Annual Review of Fluid Mechanics*, **27**, 293–334.
- Dowling, T. E., and A. P. Ingersoll, 1989: Jupiter's Great Red Spot as a shallow water system. *Journal of Atmospheric Sciences*, **46**, 3256–3278.
- Dowling, T. E., A. S. Fischer, P. J. Gierasch, J. Harrington, R. P. Lebeau, and C. M. Santori, 1998: The Explicit Planetary Isentropic-Coordinate (EPIC) Atmospheric Model. *Icarus*, **132**, 221–238.
- Farge, M., and R. Sadourny, 1989: Wave-vortex dynamics in rotating shallow water. *Journal of Fluid Mechanics*, **206**, 433–462.
- Galperin, B., S. Sukoriansky, N. Dikovskaya, P. L. Read, Y. H. Yamazaki, and R. Wordsworth, 2006: Anisotropic turbulence and zonal jets in rotating flows with a β -effect. *Nonlinear Processes in Geophysics*, **13**, 83–98.
- Gierasch, P. J., 2004: Stability of jets on Jupiter and Saturn. *Icarus*, **167**, 212–219.
- Gierasch, P. J., J. A. Magalhaes, and B. J. Conrath, 1986: Zonal mean properties of Jupiter's upper troposphere from Voyager infrared observations. *Icarus*, **67**, 456–483.
- Gierasch, P. J., et al., 2000: Observation of moist convection in Jupiter's atmosphere. *Nature*, **403**, 628–630.
- Gill, A. E., 1982: *Atmosphere-Ocean Dynamics*. Academic Press.

- Hsu, Y.-J. G., and A. Arakawa, 1990: Numerical modeling of the atmosphere with an isentropic vertical coordinate. *Monthly Weather Review*, **118**, 1933–1959.
- Huang, H.-P., and W. A. Robinson, 1998: Two-Dimensional Turbulence and Persistent Zonal Jets in a Global Barotropic Model. *Journal of Atmospheric Sciences*, **55**, 611–632.
- Huang, H.-P., B. Galperin, and S. Sukoriansky, 2001: Anisotropic spectra in two-dimensional turbulence on the surface of a rotating sphere. *Physics of Fluids*, **13**, 225–240.
- Hueso, R., A. Sanchez-Lavega, and T. Guillot, 2002: A model for large-scale convective storms in Jupiter. *J. Geophys. Res.*, **107(E10)**, Art. 5075.
- Iacono, R., M. V. Struglia, and C. Ronchi, 1999a: Spontaneous formation of equatorial jets in freely decaying shallow water turbulence. *Physics of Fluids*, **11**, 1272–1274.
- Iacono, R., M. V. Struglia, C. Ronchi, and S. Nicastro, 1999b: High-resolution simulations of freely decaying shallow-water turbulence on a rotating sphere. *Nuovo Cimento C Geophysics Space Physics C*, **22**, 813–821.
- Ingersoll, A. P., R. F. Beebe, J. L. Mitchell, G. W. Garneau, G. M. Yagi, and J.-P. Muller, 1981: Interaction of eddies and mean zonal flow on Jupiter as inferred from Voyager 1 and 2 images. *J. Geophys. Res.*, **86**, 8733–8743.
- Ingersoll, A. P., P. J. Gierasch, D. Banfield, A. R. Vasavada, and A3 Galileo Imaging Team, 2000: Moist convection as an energy source for the large-scale motions in Jupiter's atmosphere. *Nature*, **403**, 630–632.
- Li, L., A. P. Ingersoll, A. R. Vasavada, C. C. Porco, A. D. del Genio, and S. P. Ewald, 2004: Life cycles of spots on Jupiter from Cassini images. *Icarus*, **172**, 9–23.
- Li, L., A. P. Ingersoll, and X. Huang, 2006: Interaction of moist convection with zonal jets on Jupiter and Saturn. *Icarus*, **180**, 113–123.

- Lian, Y., A. P. Showman, and P. J. Gierasch, 2006: Deep jets on gas giant planets. *Eos Trans. AGU Ocean Sciences Meeting Supplement* (Honolulu, Hawaii, Feb 20-24 2006), **87(36)**, OS45L–11.
- Little, B., C. D. Anger, A. P. Ingersoll, A. R. Vasavada, D. A. Senske, H. H. Breneman, W. J. Borucki, and The Galileo SSI Team, 1999: Galileo Images of Lightning on Jupiter. *Icarus*, **142**, 306–323.
- Mac Low, M.-M., and A. P. Ingersoll, 1986: Merging of vortices in the atmosphere of Jupiter - an analysis of Voyager images. *Icarus*, **65**, 353–369.
- Magalhães, J. A., A. Seiff, and R. E. Young, 2002: The Stratification of Jupiter's Troposphere at the Galileo Probe Entry Site. *Icarus*, **158**, 410–433.
- Manfroi, A. J., and W. R. Young, 1999: Slow evolution of zonal jets on the beta plane. *J. Atmos. Sci.*, **56**, 784–800.
- Marcus, P. S., 1988: Numerical simulation of Jupiter's Great Red Spot. *Nature*, **331**, 693–696.
- Marcus, P. S., 1990: Vortex dynamics in a shearing zonal flow. *J. Fluid Mech.*, **215**, 393–430.
- Marcus, P. S., T. Kundu, and C. Lee, 2000: Vortex dynamics and zonal flows. *Physics of Plasmas*, **7**, 1630–1640.
- Nakajima, K., S.-i. Takehiro, M. Ishiwatari, and Y.-Y. Hayashi, 2000: Numerical modeling of Jupiter's moist convection layer. *Geophys. Res. Lett.*, **27**, 3129–3132.
- Nozawa, T., and S. Yoden, 1997: Formation of zonal band structure in forced two-dimensional turbulence on a rotating sphere. *Physics of Fluids*, **9**, 2081–2093.
- Okuno, A., and A. Masuda, 2003: Effect of horizontal divergence on the geostrophic turbulence on a beta-plane: Suppression of the Rhines effect. *Physics of Fluids*, **15**, 56–65.
- Panetta, R. L., 1993: Zonal Jets in Wide Baroclinically Unstable Regions: Persistence and Scale Selection. *Journal of Atmospheric Sciences*, **50**, 2073–2106.

- Peixoto, J. P., and A. H. Oort, 1992: *Physics of Climate*. American Institute of Physics, New York.
- Peltier, W. R., and G. R. Stuhne, 2002: *Meteorology at the Millennium*. International Geophysics Series, Vol. 83, Academic Press, San Diego (R.P. Pearce, Ed.), pp. 43-61.
- Polvani, L. M., J. C. McWilliams, M. A. Spall, and R. Ford, 1994: The coherent structures of shallow-water turbulence: Deformation-radius effects, cyclone/anticyclone asymmetry and gravity-wave generation. *Chaos*, **4**, 177–186.
- Porco, C. C., et al., 2003: Cassini Imaging of Jupiter's Atmosphere, Satellites, and Rings. *Science*, **299**, 1541–1547.
- Porco, C. C., et al., 2005: Cassini Imaging Science: Initial Results on Saturn's Atmosphere. *Science*, **307**, 1243–1247.
- Rhines, P. B., 1975: Waves and turbulence on a beta-plane. *Journal of Fluid Mechanics*, **69**, 417–443.
- Salyk, C., A. P. Ingersoll, J. Lorre, A. R. Vasavada, S. Ewald, and A. D. Del Genio, 2006: Interaction between eddies and mean flow in Jupiter's atmospheres: analysis of Cassini imaging data. *Icarus*, in press.
- Scott, R. K., and L. Polvani, 2006: Forced-dissipative shallow water turbulence on the sphere: equatorial confinement of zonal jets. Submitted to *J. Atmos. Sci.*
- Showman, A. P., and T. E. Dowling, 2000: Nonlinear simulations of Jupiter's 5-micron hot spots. *Science*, **289**, 1737–1740.
- Showman, A. P., and A. P. Ingersoll, 1998: Interpretation of Galileo Probe data and implications for Jupiter's dry downdrafts. *Icarus*, **132**, 205–220.
- Showman, A. P., P. J. Gierasch, and Y. Lian, 2006: Deep zonal winds can result from shallow driving in a giant-planet atmosphere. *Icarus*, **182**, 513–526.

- Smith, K. S., 2004: A local model for planetary atmospheres forced by small-scale convection. *J. Atmos. Sciences*, **61**, 1420–1433.
- Smith, K. S., G. Boccaletti, C. C. Henning, I. Marinov, C. Y. Tam, I. M. Held, and G. K. Vallis, 2002: Turbulent diffusion in the geostrophic inverse cascade. *Journal of Fluid Mechanics*, **469**, 13–48.
- Spall, M. A., and J. C. McWilliams, 1992: Rotational and gravitational influences on the degree of balance in the shallow-water equations. *Geophys. Astrophys. Fluid Dynamics*, **64**, 1–29.
- Stegner, A., and D. G. Dritschel, 2000: Numerical investigation of the stability of isolated shallow water vortices. *J. Phys. Oceanogr.* , **30**, 2562–2573.
- Sukoriansky, S., N. Dikovskaya, and B. Galperin, 2007: On the "arrest" of inverse energy cascade and the Rhines scale. *J. Atmos. Sci.*, *in press*.
- Theiss, J., 2004: Equatorward energy cascade, critical latitude, and the predominance of cyclonic vortices in geostrophic turbulence. *J. Phys. Oceanogr.* , **34**(7), 1663–1678.
- Vasavada, A. R., and A. P. Showman, 2005: Jovian atmospheric dynamics: an update after Galileo and Cassini. *Reports of Progress in Physics*, **68**, 1935–1996.
- Vasavada, A. R., S. M. Hörst, M. R. Kennedy, A. P. Ingersoll, C. C. Porco, A. D. Del Genio, and R. A. West, 2006: Cassini imaging of Saturn: southern-hemisphere winds and vortices. *J. Geophys. Res.*, **111**, E05004(E10), 1–13.
- Williams, G. P., 1978: Planetary circulations. I - Barotropic representation of Jovian and terrestrial turbulence. *Journal of Atmospheric Sciences*, **35**, 1399–1426.
- Williams, G. P., 1979: Planetary circulations. II - The Jovian quasi-geostrophic regime. *Journal of Atmospheric Sciences*, **36**, 932–968.
- Williams, G. P., 2003: Jovian Dynamics. Part III: Multiple, Migrating, and Equatorial Jets. *Journal of Atmospheric Sciences*, **60**, 1270–1296.

Yoden, S., and M. Yamada, 1993: A Numerical Experiment on Two-Dimensional Decaying Turbulence on a Rotating Sphere. *Journal of Atmospheric Sciences*, **50**, 631–644.

Young, W. R., and A. F. Thompson, 2006: Beta plane jets and equilibration of baroclinic eddies. *Eos Trans. AGU Ocean Sciences Meeting Supplement* (Honolulu, Hawaii, Feb 20-24 2006), **87(36)**, OS42F-01.

Yuan, L., and K. Hamilton, 1994: Equilibrium dynamics in a forced-dissipative f-plane shallow-water system. *Journal of Fluid Mechanics*, **280**, 369–394.

Printed December 5, 2006.

Figure Captions

FIG. 1. Layer thickness (greyscale) and winds (arrows) at 14, 139, 600, 1400, and 4190 Earth days for simulation A1, which has $r_{\text{storm}} = 0.7^\circ$, $\tau_{\text{APE}} \rightarrow \infty$, $s_{\text{max}} = 0.333 \text{ m}^2 \text{ sec}^{-3}$, $\tau_{\text{storm}} = 10^5 \text{ sec}$, and $\tau_{\text{interval}} = 1.25 \times 10^4 \text{ sec}$. Resolution is 512×298 . The midlatitude flow becomes dominated by vortices rather than jets. Because the thickness variations become large, it is difficult to see the injected mass pulses in the height field at late times, but they remain evident in the relative vorticity and divergence fields (see Fig. 2). From the top to bottom panels, the range of gh is $0.56\text{--}0.78 \times 10^5$, $0.42\text{--}0.92 \times 10^5$, $0.25\text{--}1.3 \times 10^5$, $0.20\text{--}1.7 \times 10^5$, and $0.21\text{--}2.7 \times 10^5 \text{ m}^2 \text{ sec}^{-2}$. From top to bottom, the maximum speeds are 35, 46, 66, 84, and 96 m sec^{-1} .

FIG. 2. Potential vorticity $(\zeta + f)/gh$, relative vorticity ζ , horizontal divergence $\nabla \cdot \mathbf{v}$, and zonal-mean zonal wind at 4030 Earth days for the simulation, A1, in Fig. 1. Note the nearly homogenized region of potential vorticity in the strip from $0\text{--}30^\circ\text{N}$ where the equatorial jets form. In the relative vorticity, anticyclones recently formed by forcing appear as small black ovals. In the divergence, active storms appear as white dots. In the zonal-wind plot, the dashed lines gives the zonally averaged wind plus or minus the root-mean-square zonal wind calculated along latitude circles. The potential vorticity ranges from 0 to $1.8 \times 10^{-8} \text{ sec m}^{-2}$, the relative vorticity ranges from -1.2×10^{-4} to $5.7 \times 10^{-5} \text{ sec}^{-1}$, and the divergence ranges from -1.9×10^{-6} to $4.9 \times 10^{-6} \text{ sec}^{-1}$.

FIG. 3. Critical latitude, below which jets dominate and above which vortices dominate, for my simulations (squares) and as predicted by Eq. 11 (dashed curve).

FIG. 4. Layer thickness (greyscale) and winds (arrows) at 5, 18, 200, and 2200 Earth days for simulation A5, which has $r_{\text{storm}} = 2.1^\circ$, $\tau_{\text{APE}} \rightarrow \infty$, $s_{\text{max}} = 0.333 \text{ m}^2 \text{ sec}^{-3}$, $\tau_{\text{storm}} = 10^5 \text{ sec}$, and $\tau_{\text{interval}} = 10^5 \text{ sec}$. Resolution is 256×149 . Mean $gh = 9 \times 10^5 \text{ m}^2 \text{ sec}^{-2}$ and midlatitude $L_d \approx 5000 \text{ km}$. From top to bottom, the range of gh is $8.98\text{--}9.08 \times 10^5$, $8.97\text{--}9.09 \times 10^5$, $8.82\text{--}9.12 \times 10^5$, and $8.67\text{--}9.20 \times 10^5 \text{ m}^2 \text{ sec}^{-2}$. From top to bottom, the maximum speeds are 7, 8, 12, and 18 m sec^{-1} .

FIG. 5. Potential vorticity (top), relative vorticity (second panel), horizontal divergence (third panel), and zonal-mean zonal wind (bottom) for simulation A5 (same as in Fig. 4), with midlatitude $L_d \approx 5000 \text{ km}$, at 2200 Earth days. The relative vorticity ranges from -1.2×10^{-5} to $4.6 \times 10^{-5} \text{ sec}^{-1}$ and the divergence ranges from -2.8×10^{-7} to $2.4 \times 10^{-7} \text{ sec}^{-1}$. In the bottom panel, the dashed curves give the zonally averaged zonal wind plus or minus the root-mean-square wind calculated along latitude circles.

FIG. 6. Ratio of zonal to domain-averaged root-mean-square zonal wind (a), layer thickness (b), potential vorticity (c), and relative vorticity (d). In each panel, the solid, dash-dot, and dotted curves denote simulations with midlatitude deformation radii of 1200 km, 3000 km, and 5000 km, respectively (simulations A1, A4, and A5). In wind, thickness, and potential vorticity, the flow becomes quite zonal except at high latitudes for the smallest value of L_d , indicating the dominance of vortices there.

FIG. 7. Ratio of root-mean-square v to root-mean-square u , which provides a measure of flow anisotropy. Each panel depicts a simulation with a different deformation radius, with dashed, dotted, and solid curves showing the state at ~ 100 , 1200, and 2800 Earth days, respectively. (a), (b), and (c) show results for midlatitude L_d of 1200 km, 3000 km, and 5000 km (simulations A1, A4, and A5), respectively.

FIG. 8. Zonal acceleration diagnostics at two times within a single simulation. Left panels: zonally averaged zonal wind, shown at 3.15 years (a) and 11.4 years (c). Right panels: zonally averaged zonal accelerations averaged over 3 years, ending at 3.15 years (b) and 11.4 years (d). On the right, solid curves give eddy-momentum convergence $-(a \cos^2 \phi)^{-1} \partial(\overline{u'v'}) \cos^2 \phi / \partial \phi$ and dashed-dot curves give zonal acceleration associated with mean-meridional circulation $f\bar{v}$. Note the near cancellation of the eddy-momentum convergence and $f\bar{v}$. This is simulation A1, the same as in Figs. 1–2.

FIG. 9. Available potential energy (solid) and kinetic energy (dash-dot) for simulations with τ_{APE} of ∞ , 10^8 sec, and 10^7 sec from top to bottom. These are simulations A3, D1a, and D1b, respectively. All three simulations use $r_{\text{storm}} = 2.1^\circ$, $s_{\text{max}} = 0.333 \text{ m}^2 \text{ sec}^{-3}$, $\tau_{\text{storm}} = 10^5$ sec, and $\tau_{\text{interval}} = 10^5$ sec.

FIG. 10. Available potential energy (a), kinetic energy (b), and mass-weighted mean wind speed (c) versus the “energy parameter,” $\tau_{\text{storm}}^2 r_{\text{storm}}^2 s_{\text{max}}^2 \tau_{\text{APE}} / \tau_{\text{interval}}$, for a series of simulations. Squares and diamonds correspond to simulations with mean gh values of $6 \times 10^4 \text{ m}^2 \text{ sec}^{-2}$ and $9 \times 10^5 \text{ m}^2 \text{ sec}^{-2}$, respectively. This figure includes all the simulations from Table 1 that have large-scale damping.

FIG. 11. Thickness (greyscale) and wind (arrows) for simulations with τ_{APE} of ∞ , 10^8 sec, and 10^7 sec from top to bottom (simulations A3, D1a, and D1b, respectively). The frames are shown at 8407, 8407, and 8409 Earth days of simulated time, respectively (more than 20,000 Jupiter rotations). In the top, gh ranges from $0.19\text{--}3.5 \times 10^5 \text{ m}^2 \text{ sec}^{-2}$ and maximum wind is 175 m sec^{-1} . In the middle, gh ranges from $0.2\text{--}1.4 \times 10^5 \text{ m}^2 \text{ sec}^{-2}$ and maximum wind is 196 m sec^{-1} . In the bottom, gh ranges from $0.46\text{--}1.2 \times 10^5 \text{ m}^2 \text{ sec}^{-2}$ and maximum wind is 122 m sec^{-1} . The resolution is 256×149 and midlatitude deformation radius $L_d \approx 1200 \text{ km}$ in all three simulations.

FIG. 12. Thickness (greyscale) and wind (arrows) for simulations with s_{\max} of 0.333, 0.1, 0.0333, and 0.00333 from top to bottom (simulations D1a, F1, F2, and F3, respectively). The frames are shown at 6762, 6759, 6759, and 6777 Earth days of simulated time, respectively (more than 16,000 Jupiter rotations). In the top, gh ranges from $0.2\text{--}1.6 \times 10^5 \text{ m}^2 \text{ sec}^{-2}$ and maximum wind is 216 m sec^{-1} . In the second panel, gh ranges from $0.39\text{--}0.77 \times 10^5 \text{ m}^2 \text{ sec}^{-2}$ and maximum wind is 67 m sec^{-1} . In the third panel, gh ranges from $0.55\text{--}0.66 \times 10^5 \text{ m}^2 \text{ sec}^{-2}$ and the maximum wind is 27 m sec^{-1} . In the bottom, gh ranges from $0.594\text{--}0.606 \times 10^5 \text{ m}^2 \text{ sec}^{-2}$ and maximum wind is 1.5 m sec^{-1} . The resolution is 256×149 in all four simulations.

FIG. 13. Thickness (greyscale) and wind (arrows) for simulations with a midlatitude deformation radius of $\sim 5000 \text{ km}$ and τ_{APE} of 10^8 sec (top) and 10^7 sec (bottom). These are simulations D2a and D2b. The frames are shown at 3007 Earth days of simulated time. In the top, gh ranges from $4.6\text{--}11.3 \times 10^5 \text{ m}^2 \text{ sec}^{-2}$ and maximum wind is 224 m sec^{-1} . In the bottom, gh ranges from $8.1\text{--}10.6 \times 10^5 \text{ m}^2 \text{ sec}^{-2}$ and maximum wind is 193 m sec^{-1} . The resolution is 256×149 in both simulations.

FIG. 14. Vorticity skewness for simulations with midlatitude deformation radius of 1200 km (top), 3000 km (middle), and 5000 km (bottom). In each panel, solid and dotted lines show identical cases except that injected mass pulses are positive and negative, respectively. These are simulations A2 and C1 (top), A4 and C2 (middle), and A5 and C3 (bottom). The dashed line indicates zero.

FIG. 15. Relative vorticity for three simulations A3, D1a, and D1b with mean $gh = 6 \times 10^4 \text{ m}^2 \text{ sec}^{-2}$ (midlatitude deformation radius 1200 km) showing the development of cyclonic rings (light) around the anticyclones (dark). Such a feature has recently been observed around Jupiter's Great Red Spot.

Tables

TABLE 1. Parameters Used in the Simulations

Run	Resolution	s_{\max} (m^2s^{-3})	r_{storm} ($^\circ$)	τ_{storm} (s)	τ_{interval} (s)	τ_{APE} (s)	gh_{eq} (m^2s^{-2})	Figures
A1	512×298	0.333	0.7	10^5	1.25×10^4	∞	6×10^4	1,2,3, 6,7,8
A2	256×149	0.1	2.1	10^5	5×10^4	∞	6×10^4	14
A3	256×149	0.333	2.1	10^5	10^5	∞	6×10^4	9a,11a,15a
A4	256×149	0.333	2.1	10^5	10^5	∞	3×10^5	6,7,14
A5	256×149	0.333	2.1	10^5	10^5	∞	9×10^5	4,5,6,7,14
D1a	256×149	0.333	2.1	10^5	10^5	10^8	6×10^4	9b,10,11b,15b
D1b	256×149	0.333	2.1	10^5	10^5	10^7	6×10^4	9c,10,11c,15c
D2a	256×149	3.33	2.1	10^5	10^5	10^8	9×10^5	10,13
D2b	256×149	3.33	2.1	10^5	10^5	10^7	9×10^5	10,13
F1	256×149	0.1	2.1	10^5	10^5	10^8	6×10^4	10,12
F2	256×149	0.0333	2.1	10^5	10^5	10^8	6×10^4	10,12
F3	256×149	0.00333	2.1	10^5	10^5	10^8	6×10^4	10,12
C1	256×149	-0.1	2.1	10^5	5×10^4	∞	6×10^4	14
C2	256×149	-0.333	2.1	10^5	10^5	∞	3×10^5	14
C3	256×149	-0.333	2.1	10^5	10^5	∞	9×10^5	14
E1	256×149	0.0333	2.1	10^5	10^5	10^7	6×10^4	10
E2	256×149	0.333	2.1	10^5	10^5	3×10^7	6×10^4	10
E3	256×149	3.33	2.1	10^5	10^5	3×10^7	9×10^5	10
E4	256×149	0.333	2.1	10^5	10^5	10^7	9×10^5	10

Figures

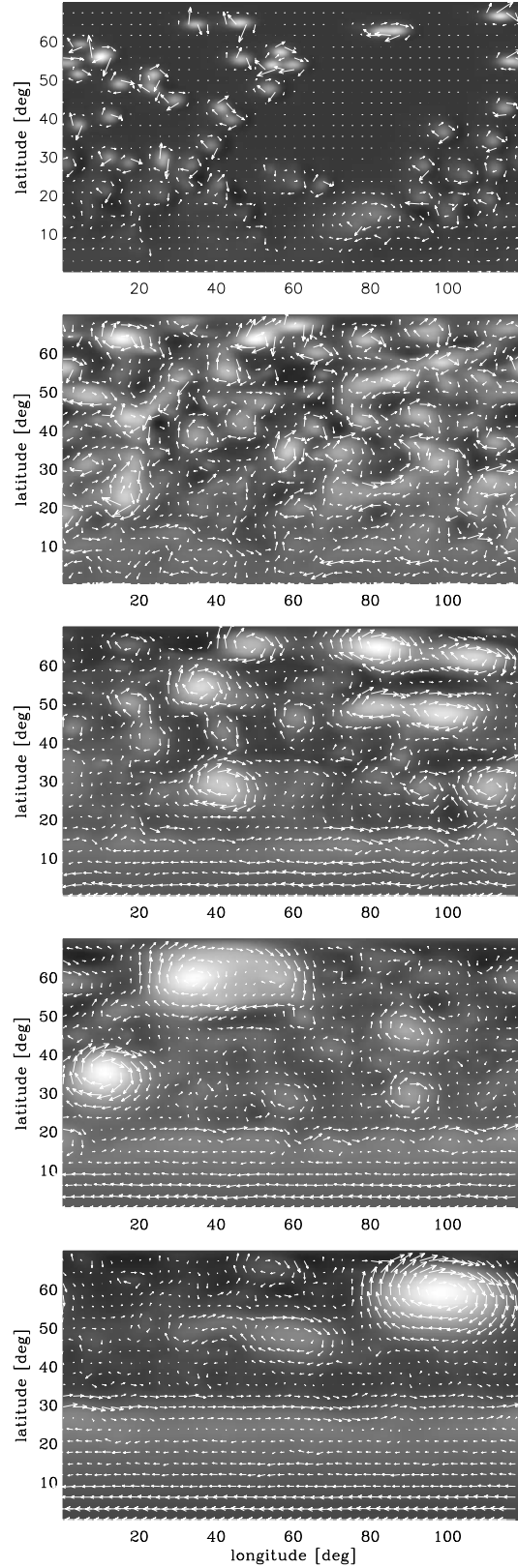


FIG. 1. Layer thickness (greyscale) and winds (arrows) at 14, 139, 600, 1400, and 4190 Earth days for simulation A1, which has $r_{\text{storm}} = 0.7^\circ$, $\tau_{\text{APE}} \rightarrow \infty$, $s_{\text{max}} = 0.333 \text{ m}^2 \text{ sec}^{-3}$, $\tau_{\text{storm}} = 10^5 \text{ sec}$, and $\tau_{\text{interval}} = 1.25 \times 10^4 \text{ sec}$. Resolution is 512×298 . The midlatitude flow becomes dominated by vortices rather than jets. Because the thickness variations become large, it is difficult to see the injected mass pulses in the height field at late times, but they remain

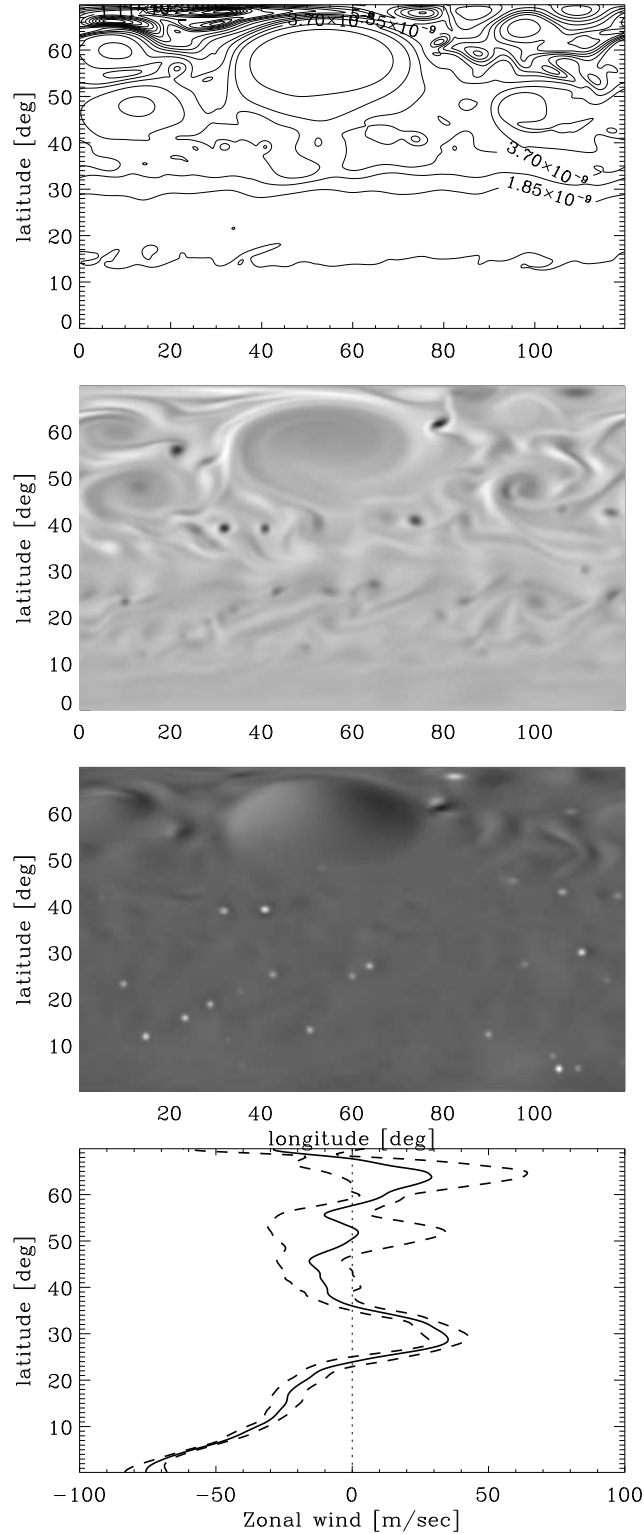


FIG. 2. Potential vorticity $(\zeta + f)/gh$, relative vorticity ζ , horizontal divergence $\nabla \cdot \mathbf{v}$, and zonal-mean zonal wind at 4030 Earth days for the simulation, A1, in Fig. 1. Note the nearly homogenized region of potential vorticity in the strip from 0–30°N where the equatorial jets form. In the relative vorticity, anticyclones recently formed by forcing appear as small black ovals. In the divergence, active storms appear as white dots. In the zonal-wind plot, the dashed lines gives the zonally averaged wind plus or minus the root-mean-square zonal wind calculated along latitude circles. The potential vorticity ranges from 0 to $1.8 \times 10^{-8} \text{ sec m}^{-2}$, the relative vorticity ranges from -1.2×10^{-4} to $5.7 \times 10^{-5} \text{ sec}^{-1}$, and the divergence ranges from $-1.0 \times$

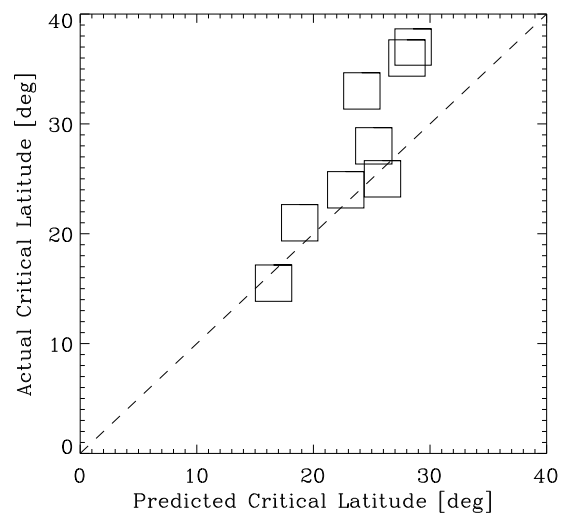


FIG. 3. Critical latitude, below which jets dominate and above which vortices dominate, for my simulations (squares) and as predicted by Eq. 11 (dashed curve).

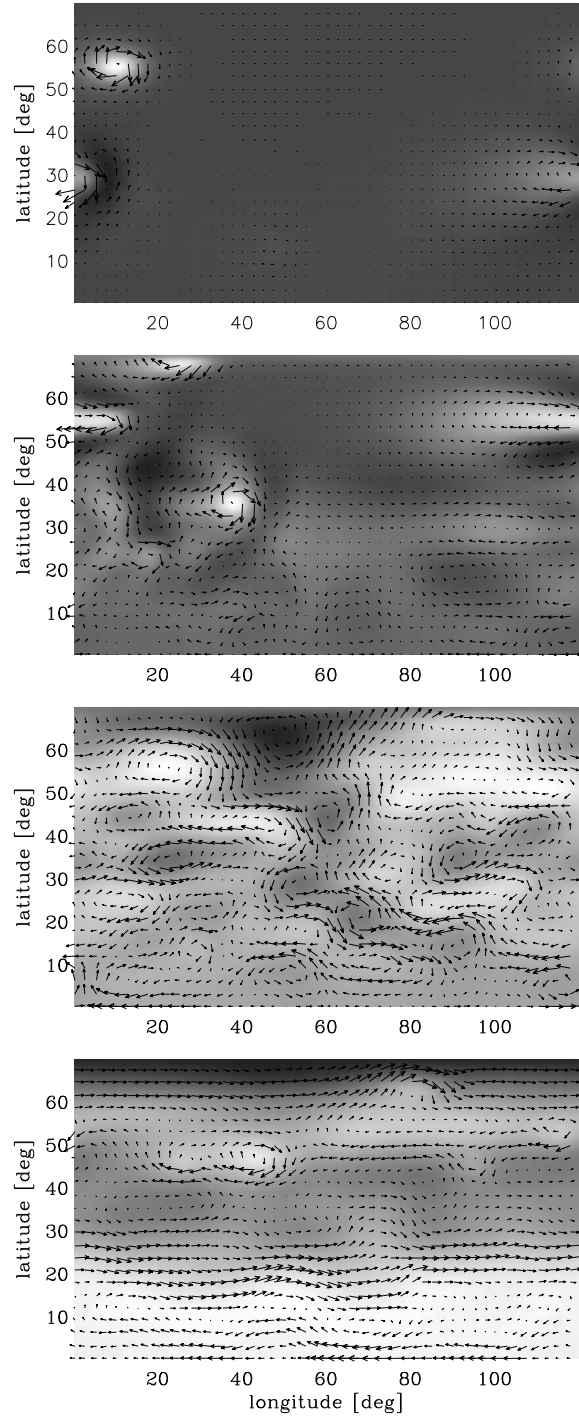


FIG. 4. Layer thickness (greyscale) and winds (arrows) at 5, 18, 200, and 2200 Earth days for simulation A5, which has $r_{\text{storm}} = 2.1^\circ$, $\tau_{\text{APE}} \rightarrow \infty$, $s_{\text{max}} = 0.333 \text{ m}^2 \text{ sec}^{-3}$, $\tau_{\text{storm}} = 10^5 \text{ sec}$, and $\tau_{\text{interval}} = 10^5 \text{ sec}$. Resolution is 256×149 . Mean $gh = 9 \times 10^5 \text{ m}^2 \text{ sec}^{-2}$ and midlatitude $L_d \approx 5000 \text{ km}$. From top to bottom, the range of gh is $8.98\text{--}9.08 \times 10^5$, $8.97\text{--}9.09 \times 10^5$, $8.82\text{--}9.12 \times 10^5$, and $8.67\text{--}9.20 \times 10^5 \text{ m}^2 \text{ sec}^{-2}$. From top to bottom, the maximum speeds are 7, 8, 12, and 18 m sec^{-1} .

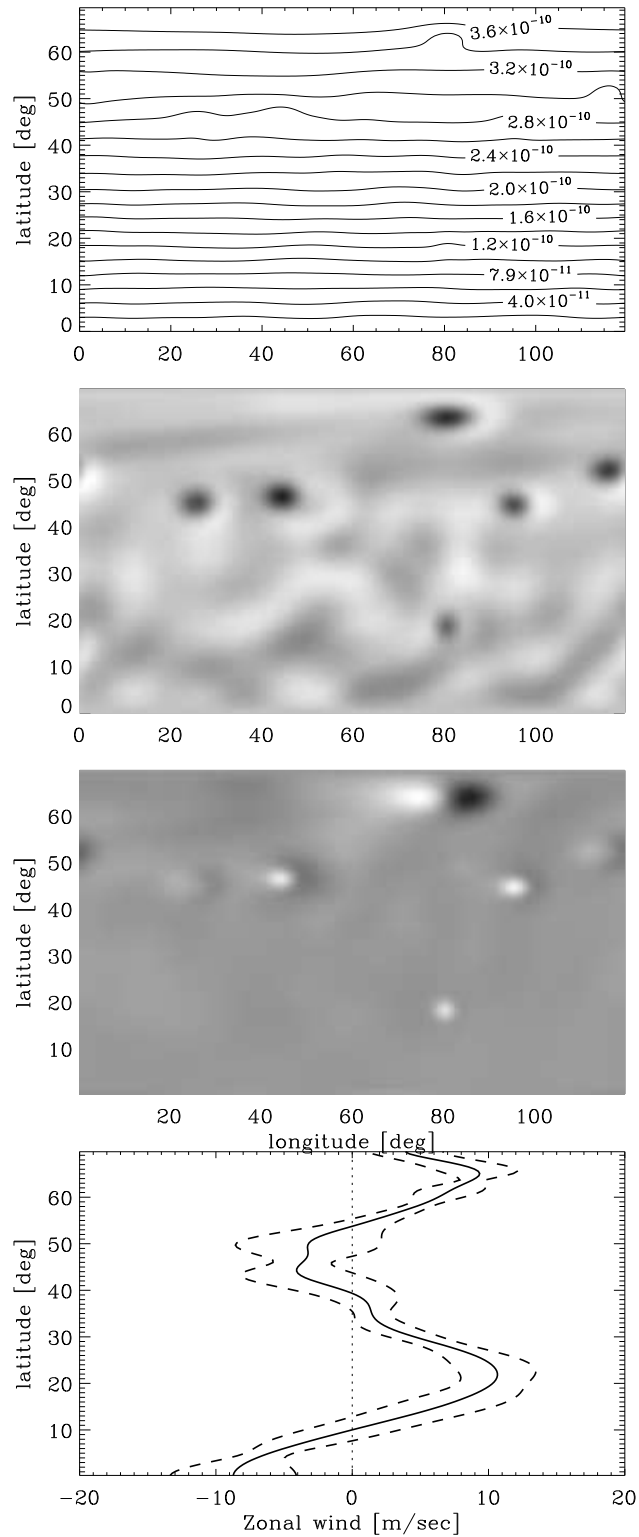


FIG. 5. Potential vorticity (top), relative vorticity (second panel), horizontal divergence (third panel), and zonal-mean zonal wind (bottom) for simulation A5 (same as in Fig. 4), with mid-latitude $L_d \approx 5000$ km, at 2200 Earth days. The relative vorticity ranges from -1.2×10^{-5} to $4.6 \times 10^{-5} \text{ sec}^{-1}$ and the divergence ranges from -2.8×10^{-7} to $2.4 \times 10^{-7} \text{ sec}^{-1}$. In the bottom panel, the dashed curves give the zonally averaged zonal wind plus or minus the root-mean-square wind calculated along latitude circles.

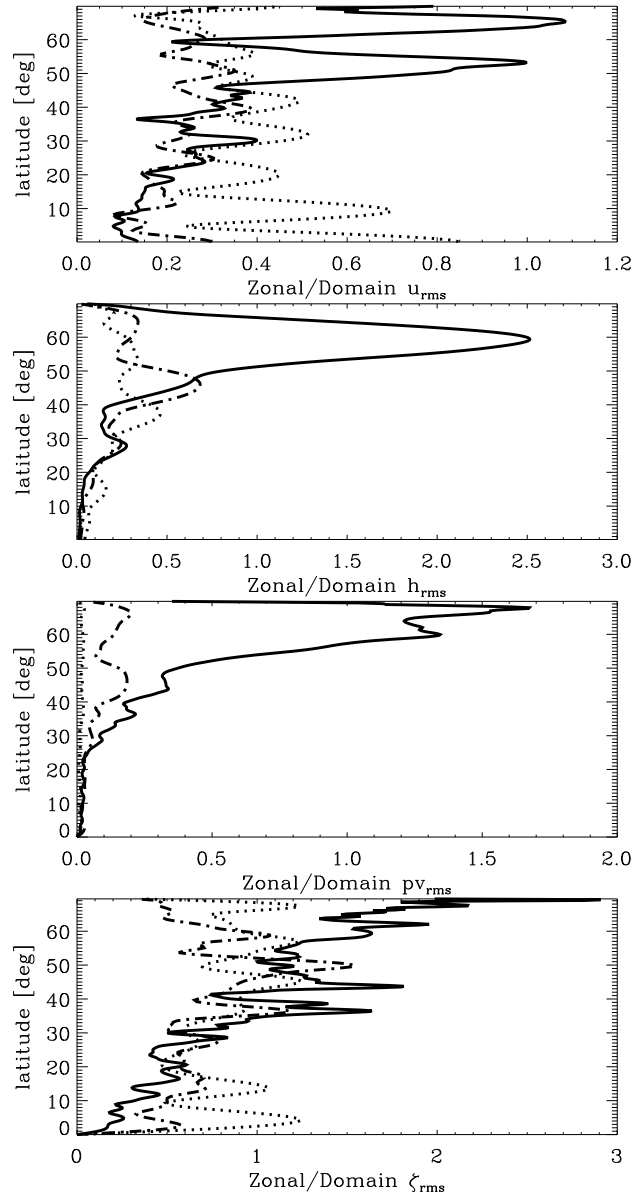


FIG. 6. Ratio of zonal to domain-averaged root-mean-square zonal wind (a), layer thickness (b), potential vorticity (c), and relative vorticity (d). In each panel, the solid, dash-dot, and dotted curves denote simulations with midlatitude deformation radii of 1200 km, 3000 km, and 5000 km, respectively (simulations A1, A4, and A5). In wind, thickness, and potential vorticity, the flow becomes quite zonal except at high latitudes for the smallest value of L_d , indicating the dominance of vortices there.

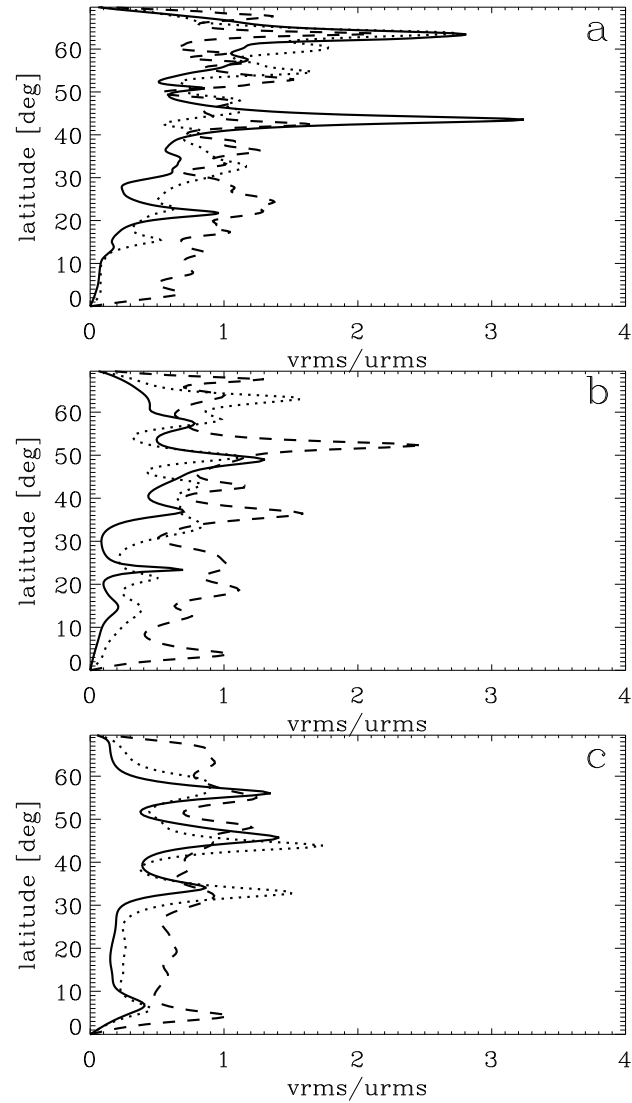


FIG. 7. Ratio of root-mean-square v to root-mean-square u , which provides a measure of flow anisotropy. Each panel depicts a simulation with a different deformation radius, with dashed, dotted, and solid curves showing the state at ~ 100 , 1200, and 2800 Earth days, respectively. (a), (b), and (c) show results for midlatitude L_d of 1200 km, 3000 km, and 5000 km (simulations A1, A4, and A5), respectively.

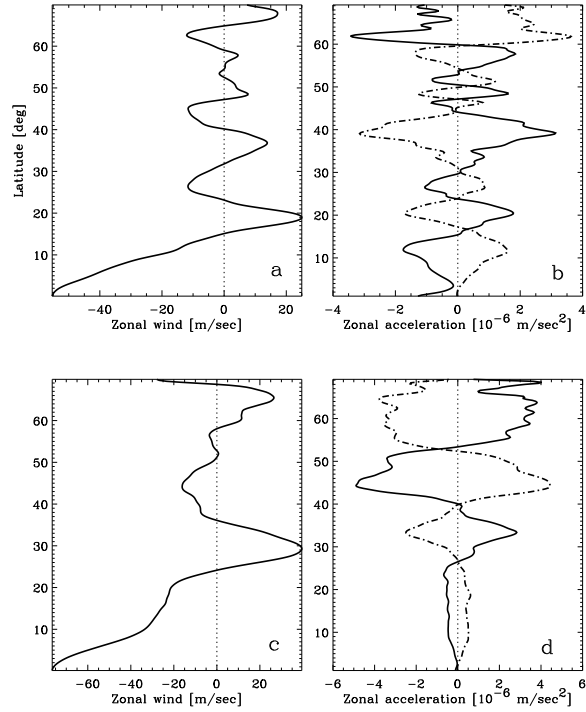


FIG. 8. Zonal acceleration diagnostics at two times within a single simulation. Left panels: zonally averaged zonal wind, shown at 3.15 years (a) and 11.4 years (c). Right panels: zonally averaged zonal accelerations averaged over 3 years, ending at 3.15 years (b) and 11.4 years (d). On the right, solid curves give eddy-momentum convergence $-(a \cos^2 \phi)^{-1} \partial(\overline{u'v'}) \cos^2 \phi / \partial \phi$ and dashed-dot curves give zonal acceleration associated with mean-meridional circulation $f\bar{v}$. Note the near cancellation of the eddy-momentum convergence and $f\bar{v}$. This is simulation A1, the same as in Figs. 1–2.

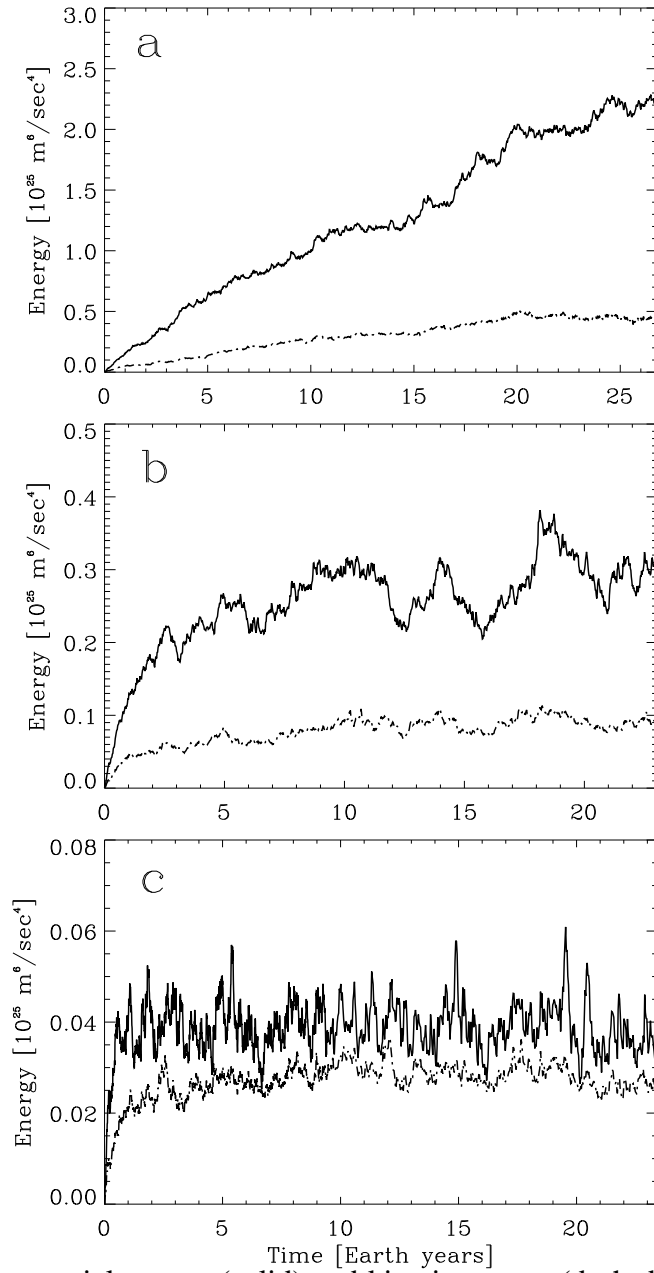


FIG. 9. Available potential energy (solid) and kinetic energy (dash-dot) for simulations with τ_{APE} of ∞ , 10^8 sec, and 10^7 sec from top to bottom. These are simulations A3, D1a, and D1b, respectively. All three simulations use $r_{\text{storm}} = 2.1^\circ$, $s_{\text{max}} = 0.333 \text{ m}^2 \text{ sec}^{-3}$, $\tau_{\text{storm}} = 10^5$ sec, and $\tau_{\text{interval}} = 10^5$ sec.

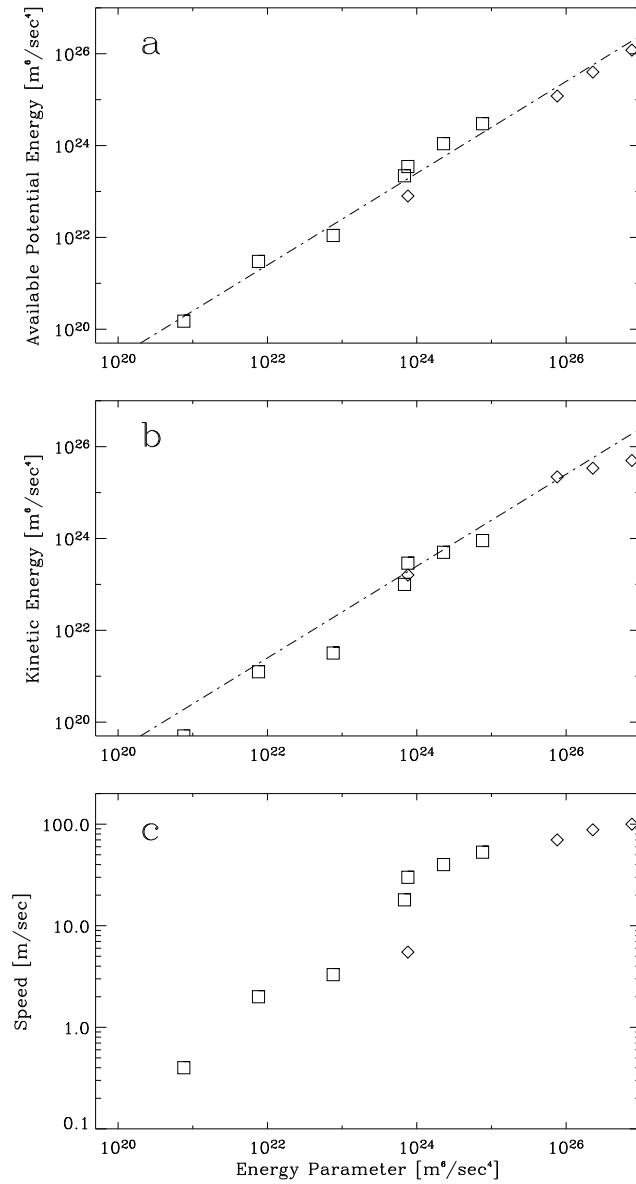


FIG. 10. Available potential energy (a), kinetic energy (b), and mass-weighted mean wind speed (c) versus the “energy parameter,” $\tau_{\text{storm}}^2 r_{\text{storm}}^2 s_{\text{max}}^2 \tau_{\text{APE}} / \tau_{\text{interval}}$, for a series of simulations. Squares and diamonds correspond to simulations with mean gh values of $6 \times 10^4 \text{ m}^2 \text{ sec}^{-2}$ and $9 \times 10^5 \text{ m}^2 \text{ sec}^{-2}$, respectively. This figure includes all the simulations from Table 1 that have large-scale damping.

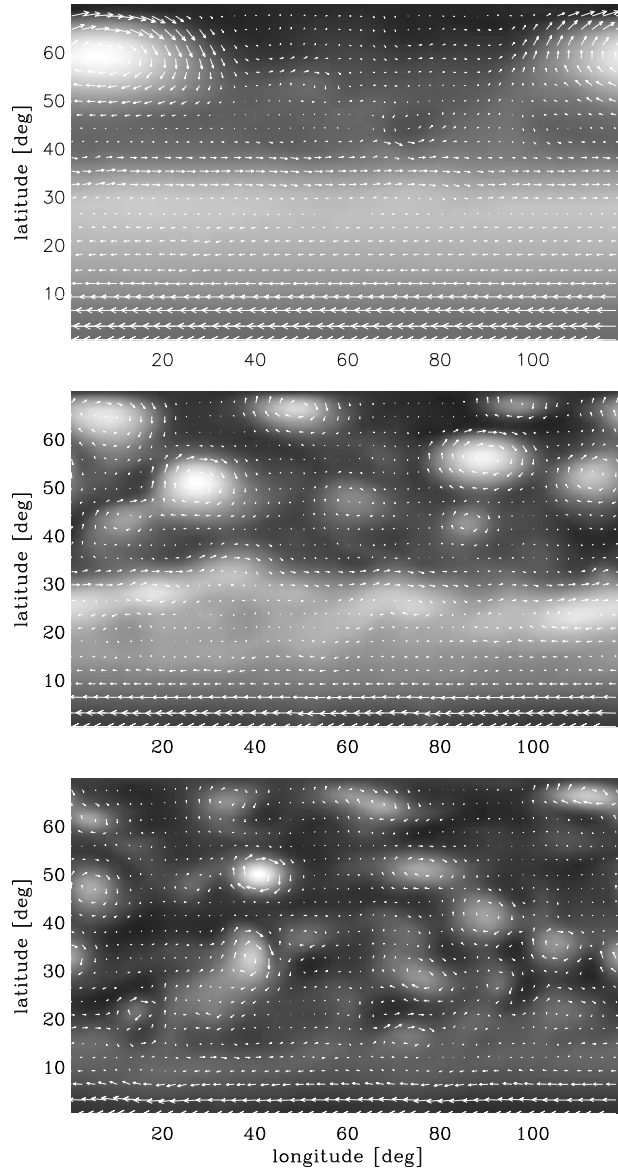


FIG. 11. Thickness (greyscale) and wind (arrows) for simulations with τ_{APE} of ∞ , 10^8 sec, and 10^7 sec from top to bottom (simulations A3, D1a, and D1b, respectively). The frames are shown at 8407, 8407, and 8409 Earth days of simulated time, respectively (more than 20,000 Jupiter rotations). In the top, gh ranges from $0.19\text{--}3.5 \times 10^5 \text{ m}^2 \text{ sec}^{-2}$ and maximum wind is 175 m sec^{-1} . In the middle, gh ranges from $0.2\text{--}1.4 \times 10^5 \text{ m}^2 \text{ sec}^{-2}$ and maximum wind is 196 m sec^{-1} . In the bottom, gh ranges from $0.46\text{--}1.2 \times 10^5 \text{ m}^2 \text{ sec}^{-2}$ and maximum wind is 122 m sec^{-1} . The resolution is 256×149 and midlatitude deformation radius $L_d \approx 1200 \text{ km}$ in all three simulations.

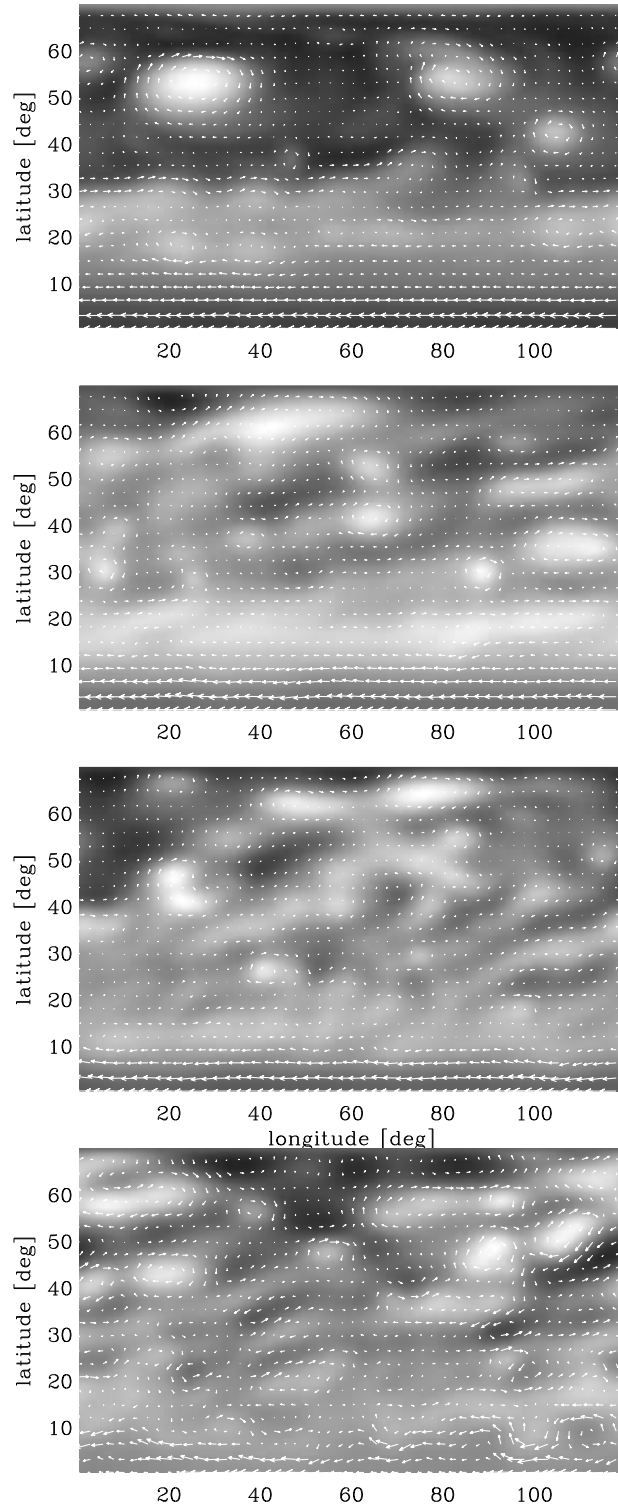


FIG. 12. Thickness (greyscale) and wind (arrows) for simulations with s_{\max} of 0.333, 0.1, 0.0333, and 0.00333 from top to bottom (simulations D1a, F1, F2, and F3, respectively). The frames are shown at 6762, 6759, 6759, and 6777 Earth days of simulated time, respectively (more than 16,000 Jupiter rotations). In the top, gh ranges from $0.2\text{--}1.6 \times 10^5 \text{ m}^2 \text{ sec}^{-2}$ and maximum wind is 216 m sec^{-1} . In the second panel, gh ranges from $0.39\text{--}0.77 \times 10^5 \text{ m}^2 \text{ sec}^{-2}$ and maximum wind is 67 m sec^{-1} . In the third panel, gh ranges from $0.55\text{--}0.66 \times 10^5 \text{ m}^2 \text{ sec}^{-2}$ and the maximum wind is 27 m sec^{-1} . In the bottom, gh ranges from $0.504\text{--}0.606 \times 10^5 \text{ m}^2 \text{ sec}^{-2}$ and maximum wind is 1.5 m sec^{-1} . The resolution is 256×140

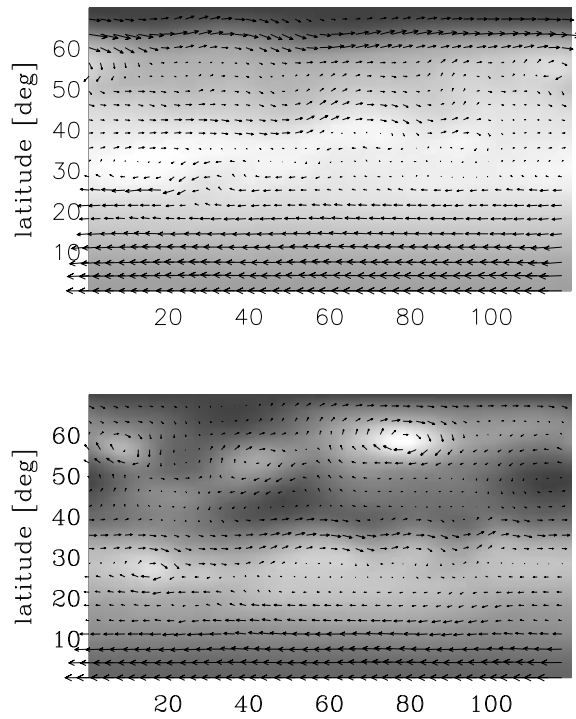


FIG. 13. Thickness (greyscale) and wind (arrows) for simulations with a midlatitude deformation radius of ~ 5000 km and τ_{APE} of 10^8 sec (top) and 10^7 sec (bottom). These are simulations D2a and D2b. The frames are shown at 3007 Earth days of simulated time. In the top, gh ranges from $4.6\text{--}11.3 \times 10^5 \text{ m}^2 \text{ sec}^{-2}$ and maximum wind is 224 m sec^{-1} . In the bottom, gh ranges from $8.1\text{--}10.6 \times 10^5 \text{ m}^2 \text{ sec}^{-2}$ and maximum wind is 193 m sec^{-1} . The resolution is 256×149 in both simulations.

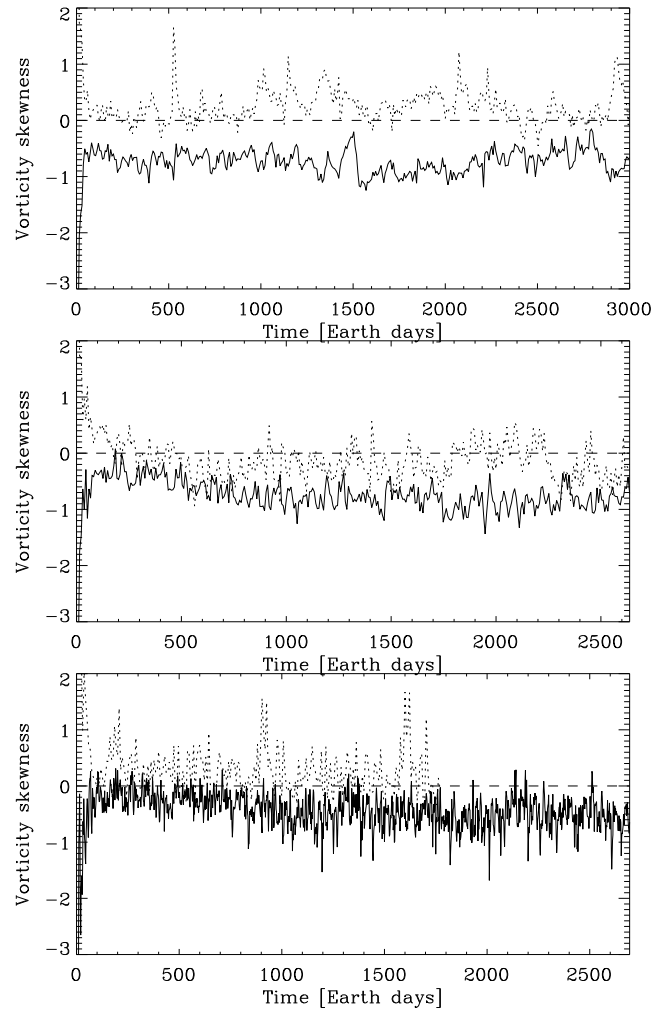


FIG. 14. Vorticity skewness for simulations with midlatitude deformation radius of 1200 km (top), 3000 km (middle), and 5000 km (bottom). In each panel, solid and dotted lines show identical cases except that injected mass pulses are positive and negative, respectively. These are simulations A2 and C1 (top), A4 and C2 (middle), and A5 and C3 (bottom). The dashed line indicates zero.

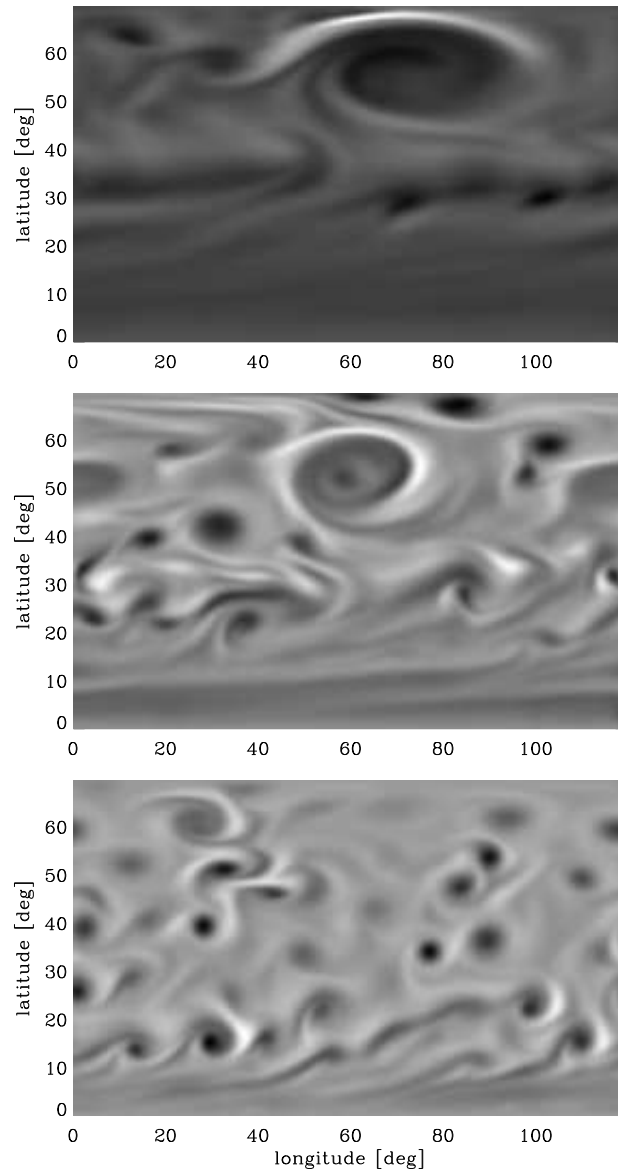


FIG. 15. Relative vorticity for three simulations A3, D1a, and D1b with mean $gh = 6 \times 10^4 \text{ m}^2 \text{ sec}^{-2}$ (midlatitude deformation radius 1200 km) showing the development of cyclonic rings (light) around the anticyclones (dark). Such a feature has recently been observed around Jupiter's Great Red Spot.